Aluminum incorporation into magnesium silicate hydrate (M-S-H)

E. Bernard, B. Lothenbach, C. Cau-Dit-Coumes, I. Pochard, D. Rentsch

Aluminum incorporation into magnesium silicate hydrate (M-S-H)

Bernard, E.[1,2)], Lothenbach, B.[1)], Cau-Dit-Coumes C.[3)], Pochard, I.[4)], Rentsch, D. [5)]

[1)] Empa, Swiss Federal Laboratories for Materials Science and Technology, Laboratory for Concrete & Construction Chemistry, 8600 Dübendorf, Switzerland
[2)] University of Bern, Institute of Geological Sciences, RWI Group, 3012 Bern, Switzerland
[3)] CEA, DEN, DE2D, SEAD, 30207 Bagnols-sur-Cèze cedex, France
[4)] UTINAM UMR 6213 CNRS, Université Bourgogne-Franche-Comté, 25030 Besançon, France
[5)] Empa, Swiss Federal Laboratories for Materials Science and Technology, Laboratory for Functional Polymers, 8600 Dübendorf, Switzerland

Corresponding author: Bernard E., email: ellina.bernard@geo.unibe.ch

Abstract

The incorporation of aluminum in magnesium silicate hydrate (M-S-H) phases was investigated. Magnesium (alumino) silicate hydrate (M-(A-)S-H) with Mg/Si ratios equal to 1.1 or 1.7 and Al/Si ranging from 0 to 0.2 were synthetized in batch experiments and equilibrated at 20, 50 and 70°C. pH values between 9 and 10.5 were observed and aluminum up to Al/Si ~ 0.15-0.18 was incorporated in M-(A-)S-H. Thermogravimetric analysis (TGA), X-ray diffraction (XRD), X-ray pair distribution function (PDF) analysis, TEM, ^{29}Si and ^{27}Al MAS NMR data showed that the M-(A-)S-H phases formed were similar to M-S-H with limited coherent size and a comparable polymerization degree of the tetrahedral silicates. Aluminum was incorporated in both tetrahedral and octahedral sites of M-S-H, while no aluminum was present as exchangeable cation on the surface sites.

1. Introduction

The formation of magnesium silicates hydrate (M-S-H) has been observed at the interfacial zone of cement-based materials in contact with clays [1-5] and/or as secondary products from the degradation of

cementitious materials by groundwater or seawater [6-8]. Magnesium silicate hydrates (M-S-H) form from the reaction of magnesium with amorphous silica released by the degradation of C-S-H at the surface of the hydrated cement [9]. SEM/EDS data indicate that aluminum could also be present either in the magnesium silicate phases [2, 4, 8] and/or in poorly crystallized hydrotalcite [1]. It remains however unclear whether aluminum is present in the magnesium silicate phases [1-8] or is found because of the intermixing with hydrotalcite-like phases, as often observed for hydrotalcite and C-S-H in hydrated cement pastes [10-12].

M-S-H phases have an ill-defined structure comparable to hydrated precursors of 2:1 and 1:1 phyllosilicates [4, 13-15]. The magnesium phyllosilicates and M-S-H are composed of tetrahedral sheets containing mainly Si^{4+} and octahedral sheets containing mainly Mg^{2+}. One tetrahedral layer over one octahedral layer corresponds to a 1:1 layer silicate structure while two tetrahedral layers sandwiching an octahedral layer correspond to a 2:1 configuration as detailed in Figure 1. Natural phyllosilicates usually contain aluminum in the tetrahedral and/or octahedral sheets. Saponite and montmorillonite are typical trioctahedral and dioctahedral smectites and are both mainly composed of magnesium, silicate and aluminum [16-19]. A negative surface charge originating from the partial substitution of Si^{4+} by Al^{3+} is typical for smectites. In the case of saponite, its negative charge is mainly due to substitutions in the tetrahedral sheets and its simplified composition can be expressed as $(Ca_{0.5}Mg_{0.5}Na{\cdot}nH_2O)_x$ $Mg_3[(Si,Al)_4O_{10}]$ $(OH)_2{\cdot}mH_2O$. In montmorillonite, a part of the Mg^{2+} of octahedral sites can be substituted by Al^{3+}: $(NaCa_{0.5}{\cdot}nH_2O)_x(Al,Mg,\square)_2[Si_4O_{10}](OH)_2{\cdot}mH_2O$, where □ is a vacant site to compensate the surplus of positive charge due to the substitution of Mg^{2+} by Al^{3+} in the octahedral layers. Therefore, only two thirds of the octahedral sites are filled. Vermiculite contains aluminum in both octahedral and tetrahedral layers: $(Ca_{0.5}Mg_{0.5}Na{\cdot}nH_2O)_x$ $(Mg,Al,\square)_3[(Al,Si)_4O_{10}](OH)_2{\cdot}mH_2O$ (where □ is a vacant site). The uptake of calcium or alkalis by M-S-H to balance the negative surface charges of the

48 silicate layers has already been reported [20, 21]. Magnesium silicate hydrate phases may thus have a
49 tendency to incorporate aluminum.

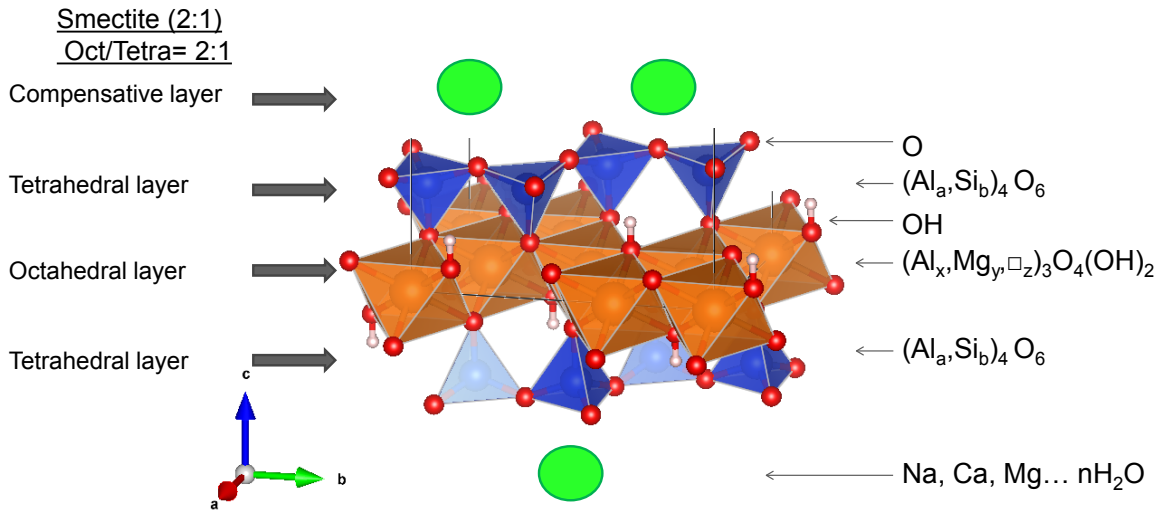

50
51 *Figure 1: Schematic sketch of phyllosilicate structure.*

52 In this work, the incorporation of aluminum in the M-S-H phases was investigated experimentally at
53 different temperatures (20, 50 and 70°C) to study the stability of M-A-S-H phases. M-A-S-H phases with
54 Mg/Si ratios of ~1.1 or 1.7 and various Al/Si ratios (Al/Si = 0, 0.05, 0.10, 0.15, and 0.20) were synthetized
55 in batch experiments by co-precipitation. The aqueous phases were analyzed by ion chromatography and
56 pH measurements and the solid phases by thermogravimetric analysis, X-ray diffraction, X-ray pair
57 distribution function (PDF) analysis, TEM, ^{29}Si and ^{27}Al MAS NMR spectroscopy. The surface charge
58 properties were analyzed by acoustophoresis measurements in the aqueous phases and cation exchange
59 capacities determinations on the solids. These experiments were supported by thermodynamic calculations
60 to better understand the MgO-Al_2O_3-SiO_2-H_2O system.

2. Materials & methods

2.1. Reagents and synthesis of M-S-H and M-A-S-H phases

Magnesium oxide (Merck, pro analysis, 0.18±0.02wt.% Na_2O, specific surface area of 24 m^2/g [22]) and silica fume (SiO_2, Aerosil 200, 0.9wt.% HCl, specific surface area of 200 m^2/g) were chosen as starting materials for the M-S-H synthesis as detailed in [22].

Metakaolin ($Al_2O_3.2SiO_2$, ARGICAL-M 1200S, purity 93.8%, specific surface area of 19 m^2/g) was added to SiO_2 and MgO to synthesize M-A-S-H samples. The XRD pattern and the ^{29}Si MAS NMR spectrum of the metakaolin powder are shown in Figure 2. This product is mainly amorphous, with small amounts of anatase, quartz, muscovite and kaolinite. The starting mixes of the M-A-S-H samples were prepared with Mg/Si ratios of 1.1 or 1.7, and Al/Si of 0.05, 0.10, 0.15 or 0.20 at liquid/solid equal to 45 with addition of milliQ water according to the amounts of MgO, SiO_2 and metakaolin summarized in Table 1.

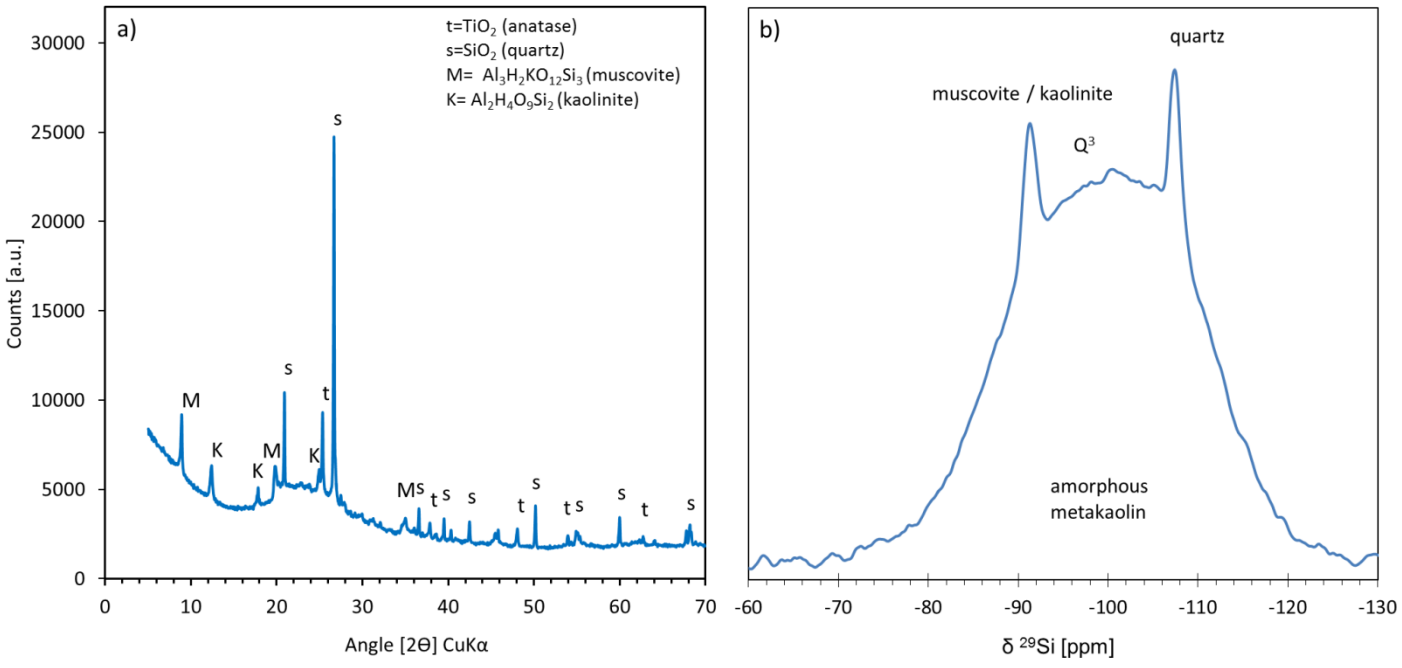

Figure 2 : a) XRD pattern and b) ^{29}Si MAS NMR spectrum of metakaolin ARGICAL-M 1200S.

Table 1: Amounts and compositions of starting materials used for the preparation of M-A-S-H=MgO + SiO_2 + metakaolin.

theoretical	M-A-S-H							
Mg/Si	1.1				1.7			
Al/Si	0.05	0.10	0.15	0.20	0.05	0.10	0.15	0.20
MgO (g)	2.09	2.04	1.99	1.95	2.59	2.54	2.49	2.45
SiO_2 (g)	2.65	2.46	2.27	2.09	2.20	2.04	1.89	1.75
$Al_2O_3.2SiO_2$ (g)	0.26	0.50	0.74	0.96	0.21	0.42	0.62	0.81

The suspensions were equilibrated at different temperatures (20, 50 and 70°C) and for different times (up to 1 or 2 years) for kinetics and thermodynamic investigations. For M-SH, similar investigations have shown that increasing the temperature does not change the type of M-S-H precipitated, but strongly increases its rate of formation [22]. Therefore, in the current paper, we focused on solid analysis of samples equilibrated for 1 year at 50°C. The solid and liquid phases were separated by filtration under pressure (4-5 bar N_2) using nylon filters (0.45 µm). Following the filtration, the solids were washed with 50/50 (volume) water-ethanol and subsequently with 94 wt% ethanol to remove dissolved ions and to prevent the precipitation of salts during drying [23]. The samples were freeze-dried with liquid nitrogen (for approximatively 20 min at -196°C) and kept at -40°C under vacuum (pressure of 0.28 mbar) for 7 days. The solid phases were analyzed after further equilibration in N_2-filled desiccators at a relative humidity of ~34% (saturated $CaCl_2$ solution) for a period of 14 days or longer to remove free water while keeping physically bound water [15]. After drying, the samples were gently ground by hand and then stored again in N_2-filled desiccators at a relative humidity of ~34%.

Pure M-S-H 1.6 was synthesized and analyzed for comparison. Previously published data on M-S-H samples [15, 24] (especially M-S-H 1.1) were also added to the manuscript.

2.2. Analytical techniques

The composition of the liquid phase was analysed by ion chromatography (IC) immediately after filtration. The dissolved concentrations of magnesium, calcium, sodium, potassium, chloride and sulphate in undiluted solutions or in solutions diluted by a factor 10, 100 or 1000 were quantified using a Dionex DP series ICS-3000 ion chromatography system with a measurement error ≤ 10%. Silicon concentrations were analyzed using sodium carbonate/bicarbonate eluent and sodium molybdate, and sodium lauryl sulfate in methanesulfonic acid as a post-column reagent using an ion pack AS22 column. Al concentrations were determined using a CS5A Dionex IonPac column with HCl diluted eluent with a post column reagent (ammonium acetate).

All concentrations were determined as duplicates and the mean values are given in the following. The pH values (accuracy = ±0.1 pH unit) were measured at ambient temperature (23±2°C) in an aliquot of unfiltered suspension and the results were corrected to 20, 50°C or 70°C, respectively [22]. The composition of the aqueous phase composition did not change significantly during the 30 minutes necessary to cool down the solutions from 50°C to ambient temperature [22].

Conventional XRD data were collected using a PANalytical X'Pert Pro MPD diffractometer equipped with a rotating sample stage in a □-2□ configuration applying CuKα radiation (λ=1.54 Å) at 45mV voltage and 40 mA intensity with step size of 0.017° 2□ and a step measurement time of 460 s, with a fixed divergence slit size and an anti-scattering slit on the incident beam of 0.5° and 1°. The samples were scanned between 5° and 75° 2□ with a X'Celerator detector.

Atomic Pair Distribution function (PDF) analysis was also performed to get information on the local structure of the M-A-S-H phases. This technique uses the entire XRD signal, including the Bragg peaks and diffuse scattering. The reduced PDF function, also known as G(r), shows the probability of finding

pairs of atoms separated by a distance r within a compound, regardless of its crystalline state. PDF analysis is thus well adapted to characterize minerals with short coherent lengths such as C-S-H, geopolymers or aluminum hydroxide gel for instance [25-27]. G(r) is obtained by taking a sine Fourier transform of the measured total scattering function S(Q), as shown in equation (1), where Q is the momentum transfer given in equation (2) with θ as the scattering angle and λ as the wavelength of the incident radiation [28].

$$G(r) = \frac{2}{\pi}\int_{Q_{min}}^{Q_{max}} Q[S(Q) - 1]\sin(Q_r)dQ \qquad (1)$$

$$Q = \frac{4\pi sin\theta}{\lambda} \qquad (2)$$

To enhance resolution after the Fourier transformation, it is important to record diffraction data with a high momentum transfer (Q). We therefore measured again the XRD patterns of selected samples using an X'Celerator Panalytical diffractometer equipped with a Mo source ($\lambda_{k_\alpha} = 0.70926$Å). The powder diffraction pattern was scanned over the 6.004-153.932° angular range with a step size of 0.0083°. Total acquisition was the average of 2 runs recorded over 24 hours each. The PDF was calculated using the PDFGetX3 software package [29]. Under our experimental conditions, the Q_{max} value was 17.3 Å^{-1}. However, the reduced structure function F(Q) = Q[S(Q)-1] exhibited strong noise at high Q values. The Fourier transform was thus calculated with Q_{max} set at 10.9 Å^{-1}. Using a finite value of Q led to the addition of spurious oscillations to G(r) depending on the r distance, which were reduced using a Lorch function [30, 31].

The ^{29}Si MAS NMR single pulse experiments were recorded on a Bruker Avance III NMR spectrometer using a 7 mm CP/MAS probe at 79.5 MHz applying the following parameters: 4500 Hz sample rotation rate, minimum of 3072 scans, 30° ^{29}Si pulse of 2.5 µs, 20 s relaxation delays, RF field strength of 33.3 kHz during SPINAL64 proton decoupling.

The ^{29}Si NMR chemical shifts were referenced to the most intense resonance at -2.3 ppm of an external sample of an octamethylsilsesquioxane (CAS Number 17865-85-9) which was referenced to tetramethylsilane (TMS, $\delta^{29}Si$ = 0.0 ppm). The observed ^{29}Si NMR signals were analysed using the Q^n classification, where a Si tetrahedron is connected to n Si tetrahedrons with n varying from 0 to 4. Severe overlap of numerous broad signals precluded the quantification of the different sites of M-A-S-H. The presence of residual unreacted metakaolin, characterized by a main resonance at -100 ppm (Figure 2b), could not be excluded, but this phase was not quantifiable by ^{29}Si NMR. As for amorphous silica (responsible for a resonance peak at 110 ppm), its presence was suspected in some of the samples only (Table 3). However, the T_1 relaxation time of silica fume can be very long and the amount of silica fume might be underestimated given our experimental conditions. Thus, this phase was not quantified [32].

The ^{27}Al NMR spectra were measured using a 2.5 mm CP/MAS probe on the same instrument. The ^{27}Al MAS NMR single pulse experiments were recorded at 104.3 MHz applying the following parameters: 25'000 Hz sample rotation rate, between 2000 and 4000 scans depending on the content of aluminum in the samples, $\pi/12$ pulses of 1.5 µs, 0.5 s relaxation delays, no ^1H decoupling. The chemical shifts of the ^{27}Al MAS NMR spectra were referenced to an external sample of $Al(acac)_3$. The ^{27}Al MAS NMR spectra were analyzed by the line shape fitting "DMFIT" software [33]. Generally the fitting of the octahedral sites was performed using i) a Lorentzian shape at 8.8 ppm (line widths of ca. 800Hz) and ii) a quadrupolar broadened shape using the "Czjzek simple" [34] model starting with the parameters: chemical shift = 11.5 ppm, FWHM CS = 2.2 ppm (full width at half maximum of the isotropic chemical shift Gaussian distribution), CQ = 4.2 MHz (peak value of the quadrupolar coupling of the Czjzek/GIM distribution) and d= 5 (exponent of the Czjzek distribution). The signals at the tetrahedral Al sites of the M-A-S-H phases were also fitted with the "Czjzek simple" model (chemical shift 68.8 ppm, FWHM CS = 7.6 ppm, CQ = 4.0 MHz and d = 5).

160 The composition of the samples is given in Table 4 and the presence of possible additional phases has
161 been investigated using the following methods: ^{29}Si MAS-NMR and ^{27}Al MAS-NMR for unreacted
162 metakaolin (< 4 wt.%), ^{29}Si MAS-NMR for amorphous silica and hydrotalcite-like phases, TGA and XRD
163 for $Mg(OH)_2$ and $Al(OH)_3$.

164 TEM characterizations were carried out on a JEOL JEM 2100F microscope operating at 200 kV and fitted
165 out with a Bruker XFlash 5030 for EDS analysis. A few milligrams of powder were vigorously mixed
166 with a few milliliters of pure ethanol in a mortar with a pestle for less than one minute. A TEM carbon-
167 covered copper grid held with tweezers was then dipped just below the ethanol surface to collect
168 suspended particles on it. The grid was then inserted in the TEM chamber and the vacuum was recovered
169 after about 15 min.

170 For the zeta potential evaluations, the experiments were carried out with non-filtered samples using
171 concentrations of 20 g of solid per liter. The suspensions were stirred in a beaker at 500 rpm during 10
172 min to reach a stable value before the measurement of the electrophoretic mobility. During the
173 measurements, stirring was set to 400 rpm and each measurement was repeated 10 times. Electrophoretic
174 mobility data were recorded with a ZetaProbe from Colloidal Dynamics Inc., which is based on the
175 frequency-dependent electroacoustic effect. Shortly, an alternating voltage is applied to the suspension
176 which causes charged particles to move back and forth at a mobility that depends on their zeta potential.
177 The software calculates the zeta potential from the frequency-dependent mobility using the O'Brien
178 equation [35]. Finally, the values obtained for each sample were background corrected with a
179 measurement of the filtrated aqueous phase.

180 Cation exchange capacities (CEC) were measured on 100 mg of powder. The cations on the surface and/or
181 from the interlayer were exchanged with cobalt hexamine trichloride (sigma-aldrich, assay: 99%) during

30 min at room temperature [1] using a solution/solid mass ratio of 30/1. The suspensions were filtered and the concentrations of Na, K, Ca, Mg, Al cations in solution were determined by ion chromatography (IC) as detailed above. The sum of measured cations was compared to the total CEC which was obtained from the difference in the cobalt hexamine concentration from the original solution and from the leachate. These concentrations were determined by colorimetry (absorption band at 473 nm) using a UNI-CAM UV visible spectrometer. The good agreement between the total CEC and the CEC calculated from the determined amounts of cations showed that dissolution of M-S-H was negligible.

2.3. Saturation indices

The calculations of the saturation indices were carried out using the Gibbs free energy minimization (GEMS) program [36]. GEMS is a broad-purpose geochemical modelling code which computes equilibrium phase assemblage and speciation in a complex chemical system from its total bulk elemental composition. The thermodynamic data for aqueous species and for brucite ($Mg(OH)_2$) were taken from the GEMS version of the PSI/Nagra thermodynamic database [37], which was completed with data relative to the M-S-H solid solution, amorphous SiO_2 [22], hydrotalcite (OH-hydrotalcite [Ht 2:1 : $Mg_4Al_2(OH)_{14}(H_2O)_3$]) [38], zeolites [39], saponite, vermiculite and montmorillonite [40] (Table 2).

As discussed in [41], amorphous or poorly ordered $Al(OH)_3$ easily precipitates in calcium sulfoaluminate cement system and a solubility product of approximately 0 ± 0.2 is initially calculated. However, the degree of ordering increases with time, and better crystalline $Al(OH)_3$ forms, while the solubility product decreases to −0.67 after 2 years, still far from the stability of the very well crystalline gibbsite. Therefore, the long curing time of our experiments (years compared to days) indicates that if aluminium hydroxide forms, a semi-amorphous or microcrystalline $Al(OH)_3$ is expected rather than a fully amorphous phase.

Consequently, the solubility product of microcrystalline aluminum hydroxide (microcrystalline $Al(OH)_3$) [42] was used in our study.

The saturation indices (SI) of the different solids were calculated based on the measured concentrations in solution according to equation (3):

$$SI = \log\frac{\mathrm{IAP}}{\mathrm{Kso}} \quad (3)$$

where IAP is the ion activity product calculated from the measured concentrations in solution, and Kso is the theoretical solubility product of the solid (Table 2).

Table 2: Standard thermodynamic properties and molar volumes of the phases considered in the study at 25 °C.

	*	$LogK_{s0}$[a]	$\Delta_f G°$ (Gibbs free energy of reaction) [kJ/mol]	V° (molar volume) [cm^3/mol]	Ref.
M-S-H (solid-solution including Ca)					
Mg/Si = 0.78	$(MgO)_{0.78}(SiO_2)_1(H_2O)_{1.48}$	-14.59	-1682.18	57	[22]
Mg/Si=1.30	$(MgO)_{1.30}(SiO_2)_1(H_2O)_{1.80}$	-21.44	-2073.47	71	[22]
Mg/Si = 0.68 Ca/Si = 0.10	$(MgO)_{0.68}(CaO)_{0.10}(SiO_2)_1(H_2O)_{1.48}$	-14.42	-1689.70	57	[20]
Mg/Si = 1.20 Ca/Si = 0.10	$(MgO)_{1.20}(CaO)_{0.10}(SiO_2)_1(H_2O)_{1.80}$	-21.57	-2082.02	73	[20]
Brucite	$Mg(OH)_2$	-11.16	−832.23	24.6	[37]
OH-hydrotalcite 2:1	$Mg_4Al_2(OH)_{14}(H_2O)_3$	-49.7	-6358.49	21.9	[38]
Microcrys. $Al(OH)_3$	$Al(OH)_3$	-0.67	-1265.28	31.95	[42]
$SiO_{2,amorphous}$	SiO_2	-2.9	-849.96	29	[22]
Montmorillonite(Mg)	$Mg_{0.17}Mg_{0.34}Al_{1.66}Si_4O_{10}(OH)_2$		-5309.00	131.6	[40]
Saponite (Mg)	$Mg_{0.17}Mg_3Al_{0.34}Si_{3.66}O_{10}(OH)_2$		-5610.70	138.6	[40]
Vermiculite (Mg)	$Mg_{0.43}Mg_{3.00}Si_{3.14}Al_{0.86}O_{10}(OH)_2$		-5742.33	139.6	[40]

[a] *All solubility products refer to the solubility with respect to the species Mg^{2+}, $Al(OH)_4^-$, $Si(OH)_4^0$, OH^-, or H_2O*

3. Results

The effect of aluminum was studied with Al/Si ratios from 0 to 0.20 at two different Mg/Si ratios: Mg/Si = 1.1 and Mg/Si = 1.7. Analyses were carried out on samples cured at 20°C for 2 years and at 50°C for 1 year. The composition of all samples is shown in Table 3, based on TGA, XRD, ^{29}Si and ^{27}Al NMR data. The solid analysis presented in the next section is focused on samples cured at 50°C for 1 year.

3.1. M-A-S-H 1.1

To mimic the pH range above 9 observed at the interface between cement and clays [1, 2] and to avoid the presence of unreacted silica or brucite, an intermediate Mg/Si ratio of ~1.1 was first investigated with variable amounts of aluminum (Al/Si 0.00 to 0.20).

The addition of a small amount of metakaolin ($Al_2O_3{\cdot}2SiO_2$) to magnesium oxide (MgO) and silica fume (SiO_2) led to the formation of magnesium silicate hydrates phases as the main product. Only little difference was observed between the TG analyses, XRD patterns and ^{29}Si MAS NMR spectra of M-(A-)S-H samples (Al/Si equal to 0, 0.05, 0.10 and 0.15) compared to pure M-S-H phases after 1 year of equilibration at 50°C, as shown in Figure 3 and Figure 4 for Al/Si = 0 and 0.10. The XRD pattern (Figure 3a) of the M-A-S-H 1.1 0.1 sample was similar to that of Al-free M-S-H: both compounds were poorly crystallized with broad reflections at 19.7, 26.7, 35.0, and 59.9 °2θ [13]. In addition, small amounts of unreacted quartz and anatase (TiO_2) already present in the metakaolin starting material (see Figure 2) were detected in sample M-A-S-H 1.1. The TGA curves (Figure 3b and Supplementary Information, Figure S1) of M-A-S-H 1.1 showed the presence of physically bound water (weight loss from 30-250°C) and structurally bound water i.e. hydroxyl groups (250-800°C) [13, 43, 44], as for M-S-H. The first water loss of M-A-S-H associated to physically bound water is slightly higher than in the M-S-H samples. This might be due i) to different relative humidities during the drying, storage or characterization processes, ii) to a true increase in the physically bound water content of M-A-S-H and/or iii) to the presence of amorphous

aluminum hydroxide gels [26]. This last hypothesis seems rather unlikely given the age of the samples (over 1 year at 50°C and 2 years at 20°C). However, the M-A-S-H 1.1 and 1.7 (see below) samples with a high alumina content possibly contained traces of semi-crystalline aluminum hydroxide possible responsible for a small water loss around 250-300°C (Supplementary Information, Figure S1). The ^{29}Si MAS NMR spectra of M-S-H and M-A-S-H both exhibited resonances at c.a. -85 ppm and between -92 and -97 ppm, assigned to Q^2 and Q^3, respectively (Figure 4), thus indicating comparable silica layer structures [13, 45]. However, the peak area ratios between the two compounds seemed to vary (for further discussion, see below). Some unreacted metakaolin could be detected with a shoulder at -100 ppm. However, quantification was very difficult due to strong overlapping.

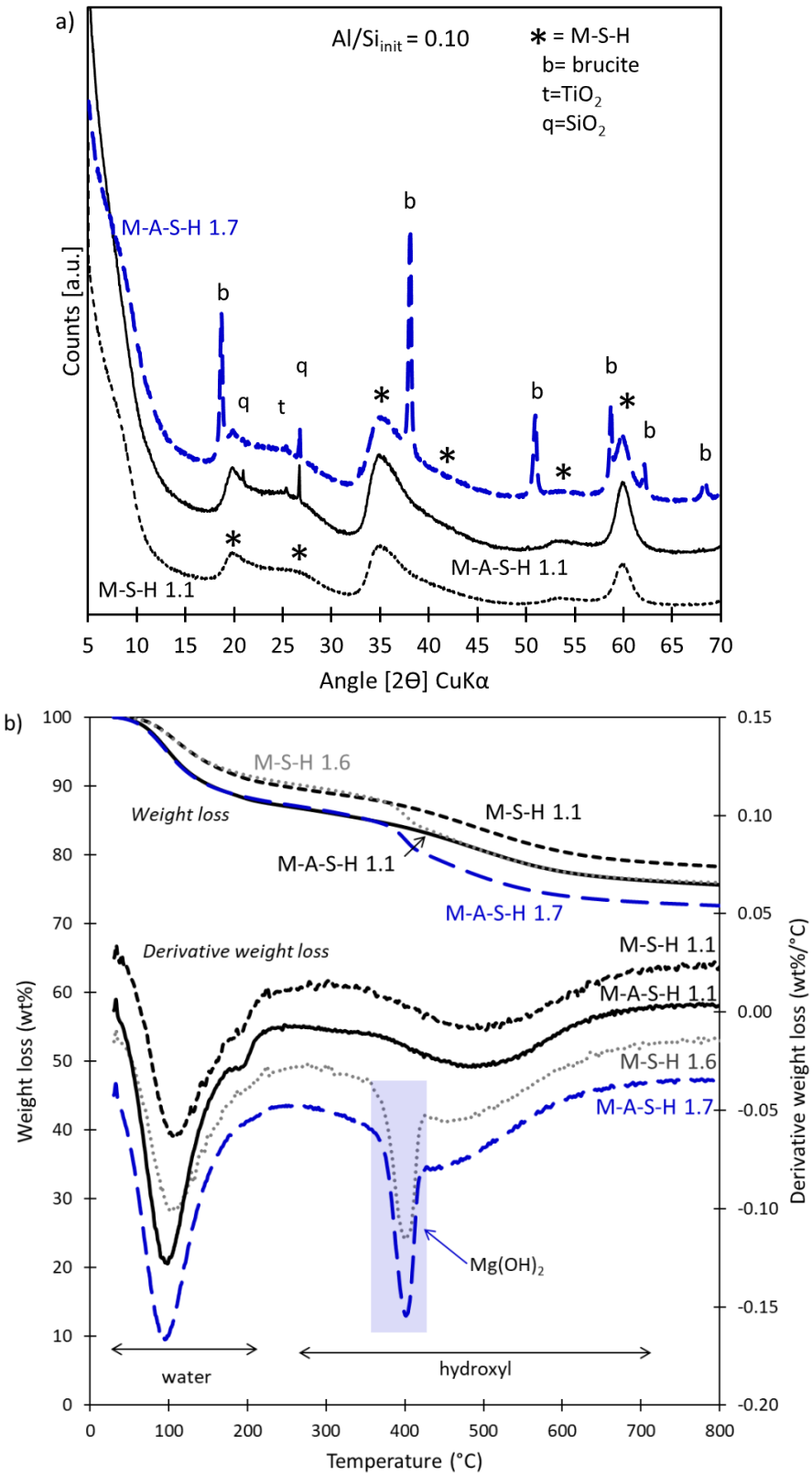

Figure 3: a) XRD patterns and b) TGA data with assignments of chemical species of M-A-S-H samples with initial Mg/Si=1.1-1-7 and Al/Si = 0.1 compared to pure M-S-H. All samples were cured 1 year at 50°C.

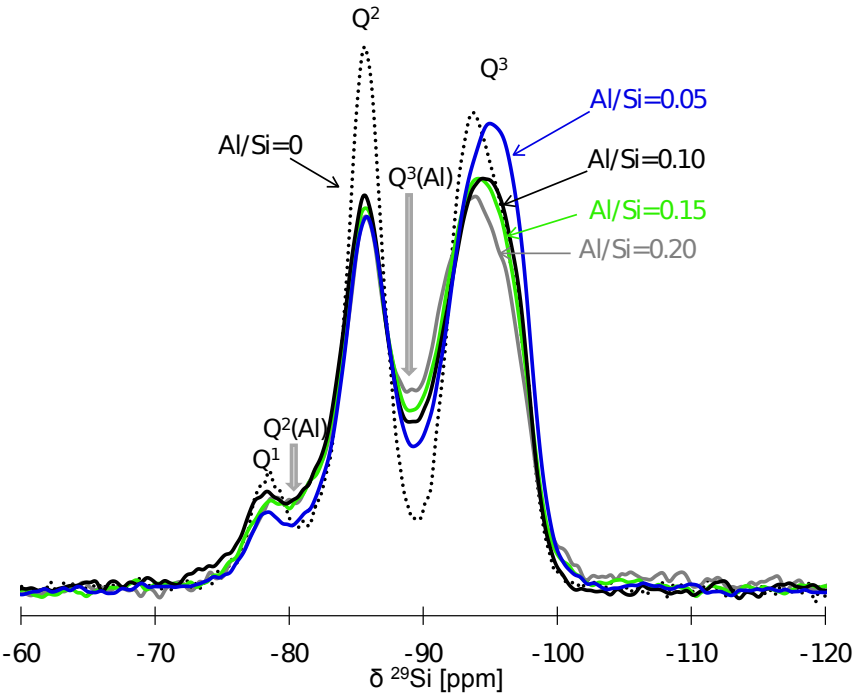

Figure 4: ^{29}Si MAS NMR spectra with assignments of Q^n environments of the M-(A-)S-H samples, Mg/Si=1.1 and Al/Si=0.05-0.20 compared to M-S-H (all samples cured for 1 year at 50°C).

After 1 year, no clear presence of brucite, aluminum hydroxide, hydrotalcite nor unreacted silica were observed in the samples synthesized at 50°C for Al/Si ratios from 0 to 0.20, as summarized in Table 3. Similar observations were made for samples synthesized and cured over 2 years at 20°C. Some unreacted silica was pointed out by ^{29}Si MAS NMR only in the sample with the highest amount of aluminum (Al/Si=0.2) (^{29}Si MAS NMR spectra shown in Supplementary Information, Figure S5 and summarized in Table 3). By TGA and XRD, a small amount of brucite was also detected in this sample (Table 3). However, in samples equilibrated at 50 and 70°C (Table 3), no silica, brucite, nor hydrotalcite were identified. This shows that the samples at 20°C were not completely at equilibrium even after 2 years of storage, as previously observed for pure M-S-H [22], while the faster kinetic at 50°C and 70°C allowed the complete reaction of silica with brucite.

Table 3: Identification of hydrotalcite, brucite and unreacted silica in the solid composition of M-(A-)S-H samples, concentrations of dissolved species, pH values of equilibrated solutions (errors: calculated Mg/Si±0.1, brucite ±2 wt%, pH ±0.1, concentrations: ±10%).

	Initial Mg/Si - Al/Si	Calculated[a] Mg/Si	Age (y)	Hydrotal.[b]	Brucite $Mg(OH)_2$	Amorphous silica	Metakaolin	Amorphous $Al(OH)_3$[b]	pH (20°C)	[Mg] mmol/l	[Si]	[Al]
20°C	1.1	*1.1*	*1*						*9.9*	*0.13*	*0.004*	---
		1.1	*2*						9.8	0.15	0.008	---
	1.1 - 0.05	*1.1*	*1*				*Tr*	*Tr*	*9.9*	*0.29*	*0.01*	*<0.0001*
		1.1	*2*				*Tr*	*Tr*	9.8	0.35	0.01	0.0005
	1.1- 0.10	*1.1*	*1*				*Tr*	*Tr*	*10.0*	*0.18*	*0.01*	*<0.0001*
		1.1	*2*				*Tr*	*Tr*	9.8	0.41	0.01	0.0002
	1.1- 0.15	*1.1*	*1*		✓		*Tr*	*Tr*	*10.0*	*0.37*	*0.02*	*<0.0001*
		1.1	*2*				*Tr*	*Tr*	9.9	0.27	0.01	0.0003
	1.1- 0.20	*n.d.*	*1*		✓	✓	*Tr*	*Tr*	*9.5*	*0.02*	*0.29*	*0.0031*
		1.2	*2*		✓	✓	*Tr*	*Tr*	9.5	0.60	0.30	0.0005
	1.6	*1.4*	*1*		✓				*10.5*	*0.12*	*0.003*	---
		1.4	*2*		✓ *(18wt%)*				10.5	0.12	0.001	---
	1.7 - 0.05	*1.4*	*1*		✓		*Tr*	*Tr*	*10.4*	*0.09*	*0.003*	*0.0007*
		1.4	*2*		✓ *(20wt%)*		*Tr*	*Tr*	10.5	0.20	0.002	0.0004
	1.7 - 0.10	*1.4*	*1*		✓		*Tr*	*Tr*	*10.5*	*0.07*	*0.005*	*0.0007*
		1.4	*2*		✓ *(20wt%)*		*Tr*	*Tr*	10.5	0.18	0.002	0.0004
	1.7 - 0.15	*1.4*	*1*		✓		*Tr*	*Tr*	*10.3*	*0.13*	*0.013*	*0.0017*
		1.4	*2*		✓ *(20wt%)*		*Tr*	*Tr*	10.5	0.11	0.003	0.0005
	1.7 - 0.20	*n.d.*	*1*		✓	✓	*Tr*	*Tr*	*9.6*	*0.12*	*0.384*	*0.0117*
		1.4	*2*	*Tr.*	✓ *(20wt%)*		*Tr*	*Tr*	10.1	0.29	0.038	0.0005
50°C	1.1	1.1	1						9.3	0.43	0.04	---
	1.1 - 0.05	1.1	1				*Tr*	*Tr*	9.3	0.36	0.01	<0.0001
	1.1 - 0.10	1.1	1				*Tr*	*Tr*	9.4	0.22	0.02	<0.0001
	1.1 - 0.15	1.1	1				*Tr*	*Tr*	9.4	0.20	0.02	<0.0001
	1.1 - 0.20	1.1	1				*Tr*	*Tr*	9.4	0.15	0.04	<0.0001
	1.6	1.4	1		✓ *(18wt%)*				10.3	0.17	0.002	---
	1.7 - 0.05	1.5	1		✓ *(20wt%)*		*Tr*	*Tr*	10.3	0.17	0.001	<0.0001
	1.7 - 0.10	1.4	1		✓ *(20wt%)*		*Tr*	*Tr*	10.4	0.09	0.001	<0.0001
	1.7 - 0.15	1.5	1	*Tr.*	✓ *(20wt%)*		*Tr*	*Tr*	10.4	0.06	0.001	<0.0001
	1.7 - 0.20	1.5	1	*Tr.*	✓ *(20wt%)*		*Tr*	*Tr*	10.5	0.03	0.001	<0.0001
70°C	1.1	1.1	1						9.2	0.29	0.005	---
	1.1 - 0.05	1.1	1				*Tr*	*Tr*	9.4	0.30	0.02	<0.0001
	1.1 - 0.10	1.1	1				*Tr*	*Tr*	9.4	0.29	0.02	<0.0001
	1.1 - 0.15	1.1	1	*Tr*			*Tr*	*Tr*	9.3	0.25	0.02	<0.0001
	1.1 - 0.20	1.1	1	*Tr*			*Tr*	*Tr*	9.5	0.20	0.02	<0.0001
	1.6	1.4	1						10.2	0.23	0.001	---
	1.7 - 0.05	1.4	1		✓ *(21wt%)*		*Tr*	*Tr*	10.3	0.21	0.001	<0.0001
	1.7 - 0.10	1.5	1		✓ *(21wt%)*		*Tr*	*Tr*	10.4	0.14	0.001	<0.0001
	1.7 - 0.15	1.5	1	*Tr*	✓ *(22wt%)*		*Tr*	*Tr*	10.4	0.10	0.001	<0.0001
	1.7 - 0.20	1.5	1	*Tr*	✓ *(23wt%)*		*Tr*	*Tr*	10.5	0.07	0.001	<0.0001

[a]Calculated = Experimentally determined ratios by mass balance corrected for the amount of brucite quantified by TGA. When amorphous silica was detected by ^{29}Si MAS NMR, the ratio was not determined (n.d.)

.[b]*Tr. = traces possibly present or cannot be excluded based on TGA and XRD data (<3wt. %).*

The high content of M-(A-)S-H phase gels, together with the trace concentrations of aluminum cations in solution (see below) and the small amount of residual metakaolin (< 4 wt.%) suggested an uptake of aluminum in M-S-H. The TEM observations of M-A-S-H sample with Mg/Si=1.1 and Al/Si=0.1 (1 year – 50°C) and the corresponding EDS measurements (Figure 5) mainly showed the formation of gels and only few analysis spots with well crystalline phases were found. The well-crystallized phases shown in Figure 5f and g mainly contained aluminum and silicon and were attributed to the presence of non-reactive phases such as kaolinite and muscovite present in the metakaolin starting material. The phases, which formed the major part, contained mainly magnesium and silicon. The observed layered texture (Figure 5a-c) was well consistent with the sheet-like morphology of pure M-S-H, confirming the similarities observed by TGA and XRD between pure M-S-H and M-A-S-H gels from this synthesis.

The Mg/Si ratio was determined for most spots in the narrow range 1.0 to 1.3 and only a few EDS measurements (Figure 5d) resulted in a slightly higher Mg/Si ratio. This higher ratio might be reached by mixing very small amounts of magnesium hydroxide with M-(A-)S-H phases or, alternatively, with a chlorite-like structure (T:O:T . O) whereby $Mg(OH)_2$-like layers (type O) are intercalated into the structure of typical phyllosilicate as talc (type T:O:T), by increasing the Mg/Si ratio in the solid [46].

A closer look at the EDS measurements in a ternary plot (Figure 5d, e) pointed towards the presence of two population measurements: one with Mg/Si ~ 1.0 ± 0.1 and Al/Si ~ 0.06, the second with Mg/Si ~ 1.3 ± 0.1 and less aluminum. These two types of elemental compositions also had a different morphology, as evidenced by the TEM pictures corresponding to the EDS measurements (Figure 5a- c): the areas with Mg/Si ~ 1.0 ± 0.1 and more aluminum consisted of thin foil-like gels (spots 2, 4-6, 11, 13, 15, 17, 19), those with Mg/Si~1.3 ± 0.1 and less aluminum of thicker fibrillary particles (spots 3, 12, 16, 18, 20). Note that the aluminum and magnesium content may also depend on the thickness of the particle investigated (spots 1, 9, 10 and 14 are not shown as they do not belong to M-A-S-H phases). Given the limited number

296 of spots, the TEM/EDS analysis results showed rather high uncertainty. The lower Al/Si content could
297 result from non-reactive Si-Al residual phases or from the formation of small amounts of amorphous
298 $Al(OH)_3$ gel, which could however not be evidenced by our experimental techniques.

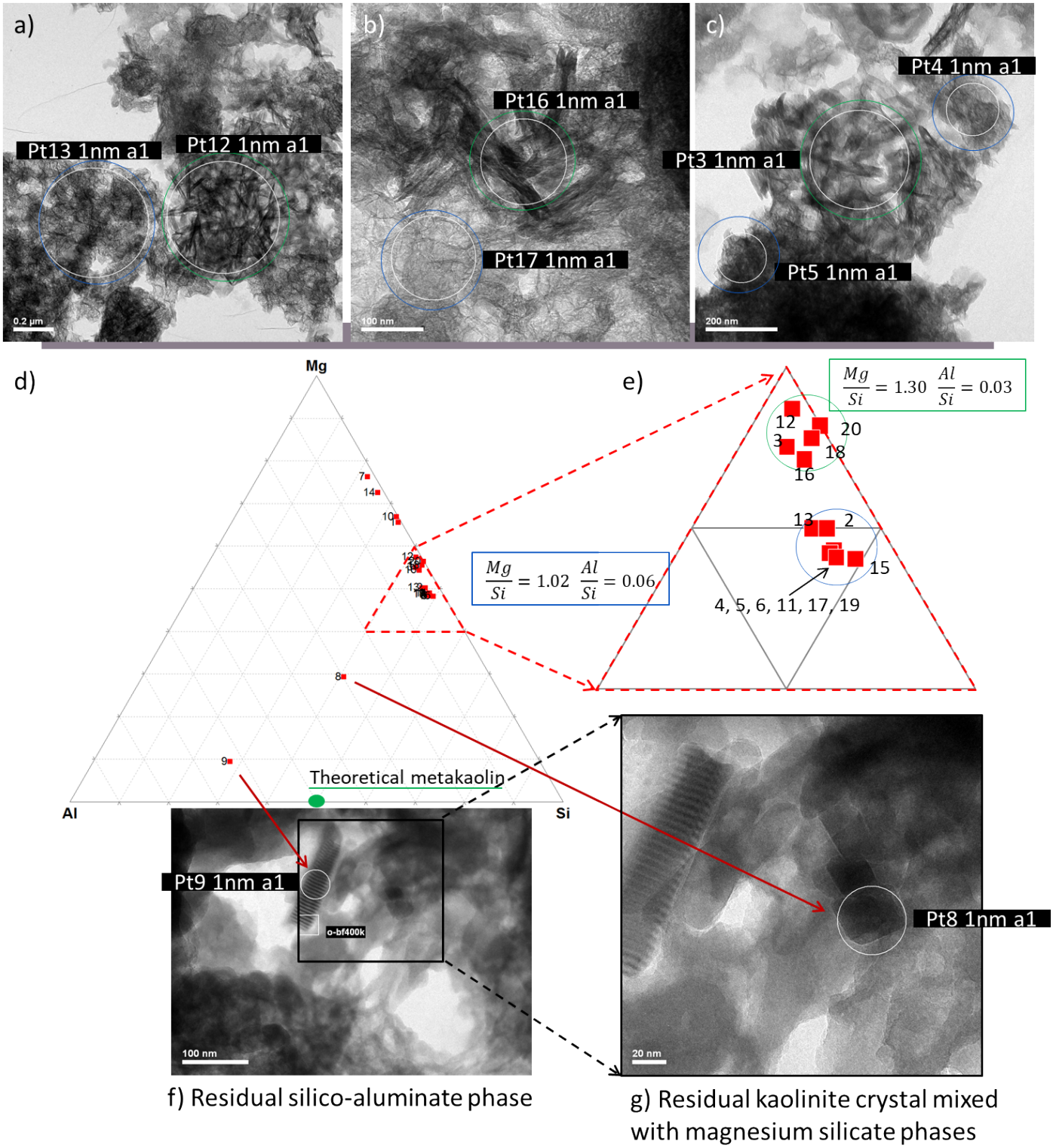

Figure 5: a, b, c) TEM images of M-A-S-H particles (Mg/Si = 1.1, Al/Si = 0.1, 1 year – 50°C), d) Al-Si-Mg ternary plots (in molar units) obtained from EDS chemical analyses with e) zoomed section; f) and g) TEM images of residual crystalline phases from metakaolin starting material.

The ^{29}Si MAS NMR spectra of the M-A-S-H 1.1 samples (Figure 4) exhibited small differences indicating structural changes of the silicate layers. In the presence of aluminum, the resonances at -85 (Q^2) and at -95 ppm (Q^3) were broadened and the relative signal intensity of the Q^2 resonance compared to the signals assigned to Q^3 was reduced (Figure 4). The relative intensities of the resonances at ~ -82 and particularly in the region of -91 ppm increased with the Al/Si ratio, showing an increase of silicate species with aluminum neighbors. It is known that the replacement of silicon by aluminum induces high frequency shifts of δ^{29}Si [47, 48]. Hence, the two resonances were assigned to Q^2(Al) at -91 ppm, i.e., silicate with one aluminate and one silicate neighbor, and to Q^3(Al) tetrahedral silicate at -82 ppm, i.e., silicate with one aluminate and two silicate neighbors, respectively. The comparison with the ^{29}Si MAS NMR spectrum of saponite (data not shown) further confirmed the assignment of the signal at ~ -91 ppm to a Q^3(Al) tetrahedral silicate site [49]. The chemical shift of silicate is mainly influenced by changes in the adjacent tetrahedral silicate layer (and only weakly by replacement in the octahedral magnesium layer [48, 50]). The observed δ^{29}Si NMR data was thus consistent with the uptake of aluminum into the silicate sheets of the M-A-S-H phase. The intensity increase of the signal at ~ -91 ppm occurred simultaneously with a slight decrease of the signal intensity at -93 to -97 ppm (Q^3), showing qualitatively that the content of silicate next to aluminum tends to increase for samples with higher aluminum contents.

^{27}Al MAS NMR spectra of M-A-S-H 1.1 (1 year – 50 °C) with different Al-contents and of the raw metakaolin starting material are shown in Figure 6. The spectra show that a large fraction of metakaolin was consumed to form the M-A-S-H phases. The ^{27}Al MAS NMR data of M-A-S-H showed the presence of large quantities of VI-fold coordinated aluminum with the signal observed at 0-20 ppm assigned to octahedrally coordinated Al(VI) environment [48, 51] and possible V-fold coordinated aluminum around 30 ppm in low quantities due to some traces of unreacted metakaolin (< 5 wt.%) or possibly due to little content V-fold coordinated aluminum in the M-A-S-H phase.

The line shape of the Al(VI) resonance was fitted by two Al(VI) sites: A Lorentzian signal centered at ~9 ppm which apparently showed a very symmetric shape and an additional, broad and asymmetric signal at ~11 ppm, which was simulated applying the "Czjzek simple" model of the "DMFIT" software (for details on the fitting process see section "2. Materials & methods") [34]. The quadrupolar broadened shape of this 2nd resonance (isotropic ^{27}Al NMR chemical shift at ~11 ppm) is related to a poor ordering of the layers [52, 53].

The Al(VI) resonance in clay mineral normally occurs at 0 - 10 ppm, depending on the structure of the octahedral sheets. In dioctahedral minerals, in which only 2 out of 3 octahedral sites are occupied, Al(VI) is close to 0 ppm, while in trioctahedral phyllosilicates, where all octahedral positions are filled, Al(VI) occurs at 5-10 ppm [48]. In several silicate-free phases, however, the Al(VI) resonance is also found at almost the same chemical shift of ~ 9-11 ppm: In hydrotalcite-like phases, a symmetrical Al(VI) signal is observed [54] and for poorly ordered aluminum hydroxide an asymmetrical signal is expected [26]. ^{27}Al MAS NMR spectra of reference samples (hydrotalcite and micro-crystalline aluminum hydroxide) are presented in the supplementary information, Figure S2.

The broad Al(VI) resonance at 0-20 ppm observed in the ^{27}Al MAS-NMR spectra of the M-A-S-H phases (Figure 6) could unfortunately not help to capture the possible trioctahedral or dioctahedral character of the non-silicate phases nor to fully clarify the total absence of non-silicate phases. The presence of hydrotalcite or aluminum hydroxide, however, seems rather unlikely as:

- these two phases could not be evidenced by TGA and XRD,
- the solutions were undersaturated with respect to both solids (as discussed below).

Therefore, the two fitted ^{27}Al NMR resonances in the current work at δ^{27}Al(VI) ~ 10-11 ppm were assigned to aluminum in the octahedral magnesium oxide sheet of M-(A-)S-H phases.

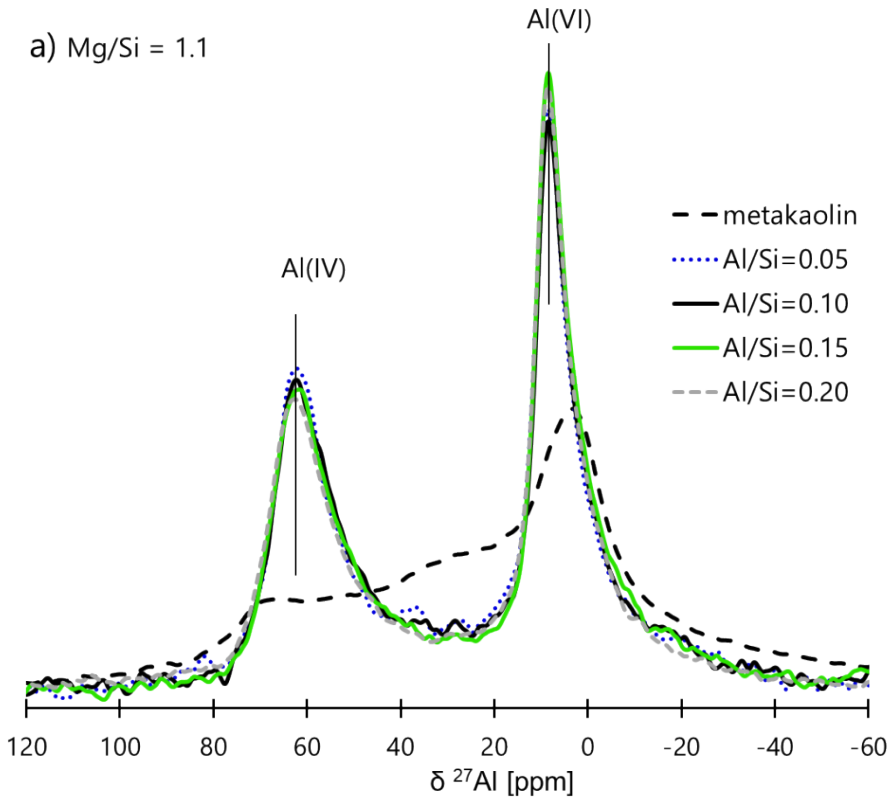
a) Mg/Si = 1.1
Al(VI)
Al(IV)
metakaolin
Al/Si=0.05
Al/Si=0.10
Al/Si=0.15
Al/Si=0.20
120
100
80
60
40
20
0
-20
-40
-60
δ 27Al [ppm]

349

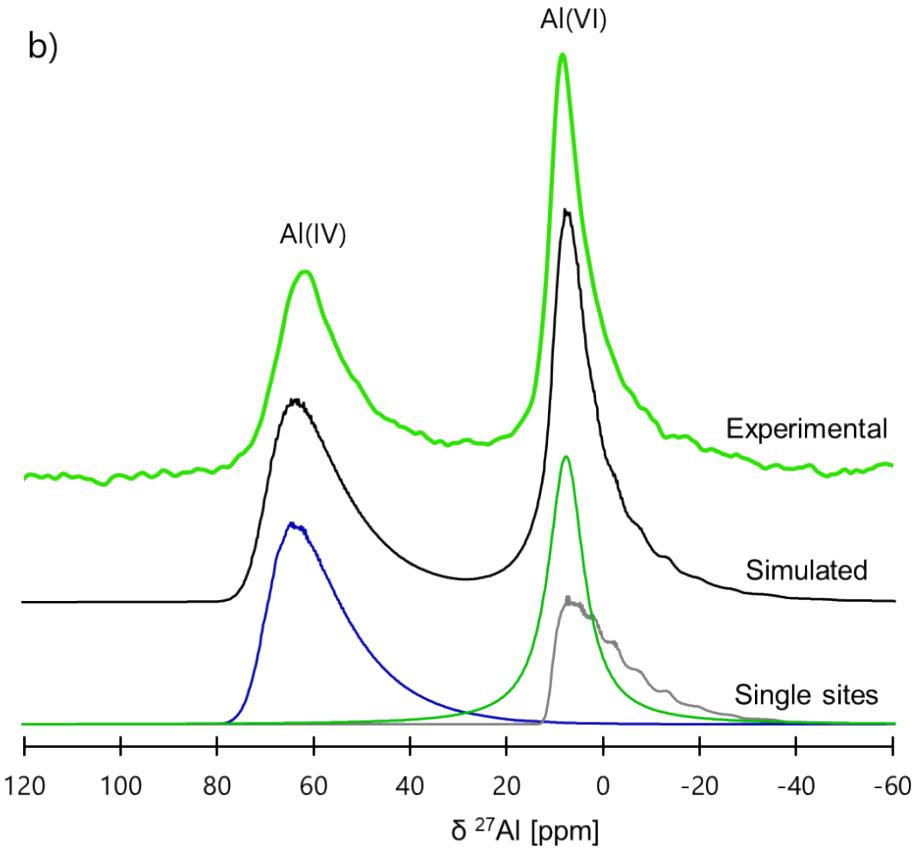
b)
Al(VI)
Al(IV)
Experimental
Simulated
Single sites
120
100
80
60
40
20
0
-20
-40
-60
δ 27Al [ppm]

350

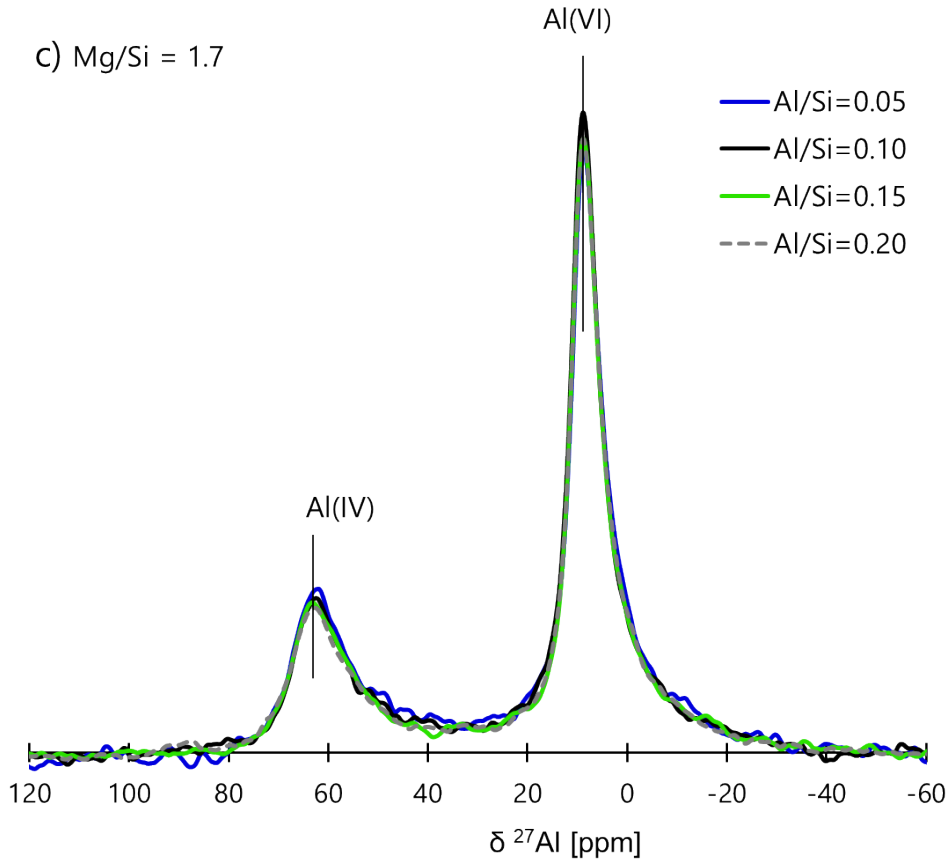

Figure 6: a) ^{27}Al MAS NMR spectra of M-A-S-H phases (1 year – 50°C), Mg/Si=1.1 and Al/Si=0.05-0.20 compared to raw metakaolin; b) example of the deconvolution (sample with Mg/Si = 1.1 and Al/Si=0.15) of the indicated single sites (Table 4), c)) ^{27}Al MAS NMR spectra of M-A-S-H phases, Mg/Si=1.7 and Al/Si=0.05-0.20.

The broad resonances with signal maxima at ~ 62 ppm in the ^{27}Al NMR spectra (Figure 6) confirmed the presence of tetrahedrally coordinated aluminum, as e.g. observed in saponite reference material ([52], data not shown). The Al(IV) signal appeared with a broad and asymmetric shape for all M-A-S-H phases and could again indicate the presence of one (or more) poorly ordered aluminum sites in the tetrahedral silicate layers [52]. We were able to simulate the tetrahedral part of all ^{27}Al MAS NMR spectra of the M-A-S-H phases by applying only one signal of the "Czjzek simple" shape and subsequently evaluated the distribution of aluminum Al(VI) and Al(IV) for all phases [33]. The most important parameters for the

deconvolutions of ^{27}Al NMR data for samples aged 2 years at 20°C and 1 year at 50°C as well as the evaluated Al(VI)/Al(IV) ratios are summarized in Table 4.

The ^{27}Al MAS NMR spectra of M-A-S-H 1.1 phases showed a fairly similar distribution of the aluminum sites in all samples: approximately 60% of the aluminum at Al(VI) sites and the remaining 40% at Al(IV) sites. This approximately 60/40% distribution of aluminum in the M-A-S-H 1.1 indicates a comparable uptake of aluminum in the octahedral magnesium oxide and tetrahedral silicate layer and thus implies no or only minor changes in the total net surface charge compared to pure M-S-H. Only negligible effects of temperature on the aluminum speciation were observed.

Finally, neglecting the possible presence of amorphous aluminum hydroxide gels and taking into account the unreacted metakaolin at a maximum of 5 wt.% in the sample, the Al/Si max was recalculated and a maximum value of 0.18 was obtained.

Table 4: Sample composition of Al (IV) and Al(VI) sites determined by line shape analysis of ^{27}Al MAS NMR data of M-A-S-H 1.1 phases and quadrupolar parameters and metakaolin quantification.

		Al(IV)		Al(VI) a			Al(VI) b[a]			
	Al/Si	δ_{iso} [ppm]	[%]	CQ* [MHz]	δ_{iso} [ppm]	Rel. amount [%]	CQ* [MHz]	δ_{iso} [ppm]	[%]	Al(VI)/Al(IV)
Mg/Si = 1.1										
20°C / 2years	0.05	69.6	36	4.09	11.6	10	4.09	9.2	53	1.8
	0.1	69.0	38	3.95	11.9	22	4.09	8.8	40	1.6
	0.15	68.9	39	3.58	11.1	16	3.58	9.1	45	1.5
50°C / 1year	0.05	68.6	40	4.13	11.6	19	4.28	8.6	41	1.5
	0.1	68.8	42	4.38	11.6	22	4.34	8.4	36	1.4
	0.15	68.9	40	4.39	11.6	26	4.38	8.5	34	1.5
	0.2	69.5	40	4.33	11.4	21	4.26	8.6	40	1.5
Average		*69.0*	*40 ± 2*		*11.5*	*19 ± 5*		*8.8*	*41 ± 4*	*1.5*
Mg/Si = 1.7										
20°C / 2years	0.05	69.1	20	4.24	11.7	18	4.41	8.9	62	4.0
	0.1	68.9	23	3.73	11.8	15	4.33	8.9	62	3.3
	0.15	68.7	27	3.68	11.8	23	4.34	8.7	50	2.7
50°C / 1year	0.05	69.1	29	4.41	11.4	21	4.35	8.7	50	2.5

	0.1	68.7	26	4.13	11.5	18	4.46	8.8	56	2.8
	0.15	68.6	26	3.96	11.8	20	4.56	8.7	54	2.9
	0.2	68.9	25	4.01	11.6	20	4.39	8.7	55	3.0
	Average	*68.9*	*25 ± 3*		*11.7*	*19 ± 3*		*8.8*	*56 ± 5*	*3.0*

δ_{iso} is the isotropic chemical shift, d_{CSA} is the full width at half maximum of Gaussian distribution of δ_{iso}, and *CQ* is the peak value of the quadrupolar coupling constant product in the "Czjzek simple" model (see 2.2)*

dCSA (Al (IV))= 7.6 ppm and dCSA (Al (VI)a)=2.2 ppm

[a]=no differentiation possible between the Lorentzian signal Al(VI) centered at ~9 ppm (symmetric shape) from hydrotalcite or from M-A-S-H

The PDF analyses of the investigated samples (Figure 7) showed similarities regardless of the Al/Si ratio. The coherence length seemed to be less than 20 Å, which is consistent with the poor crystallinity of the products. In a previous work [15], the peaks of M-S-H were tentatively assigned using the structures of talc [55] and antigorite [56] as reference material: they mainly corresponded to Mg-Mg (r = 3.1 Å, 5.4 Å, 8.2 Å, 9.4 Å, 11.1 Å) and Mg-O (2.1 Å) distances within the same layer as well as Si-Si (3.2 Å) and Si-O distances in tetrahedral silicate layer (r = 1.6 Å). Note that peaks below 1.5 Å caused by imperfect corrections and termination errors are not meaningful. The correlation peaks at 1.6 Å (Si-O) seemed to be slightly shifted towards higher r values with increasing the Al/Si ratios (Figure 7-b). In tetrahedral coordination, the Al-O bond (typically ≈1.75 Å) is longer than the Si-O bond (≈1.60 Å) [57-59]. As for distances reported for Al-O bonds in octahedral environment, they are usually close to 1.9-2.0 Å (1.89 – 1.92 Å for well-ordered Al in kaolinite, and slightly higher values (1.97 Å and 2.05 Å) in distorted octahedral [60], 1.92 Å in grossular [61], 1.90 Å in gibbsite [62], ≈ 1.90 Å in ettringite [63]. The observation of slightly larger r values for samples with elevated Al/Si ratios might thus result from a contribution of Al-O distances (in tetrahedral and octahedral environments), which would be consistent with an uptake of Al in the main layers and would agree well with ^{27}Al MAS NMR results.

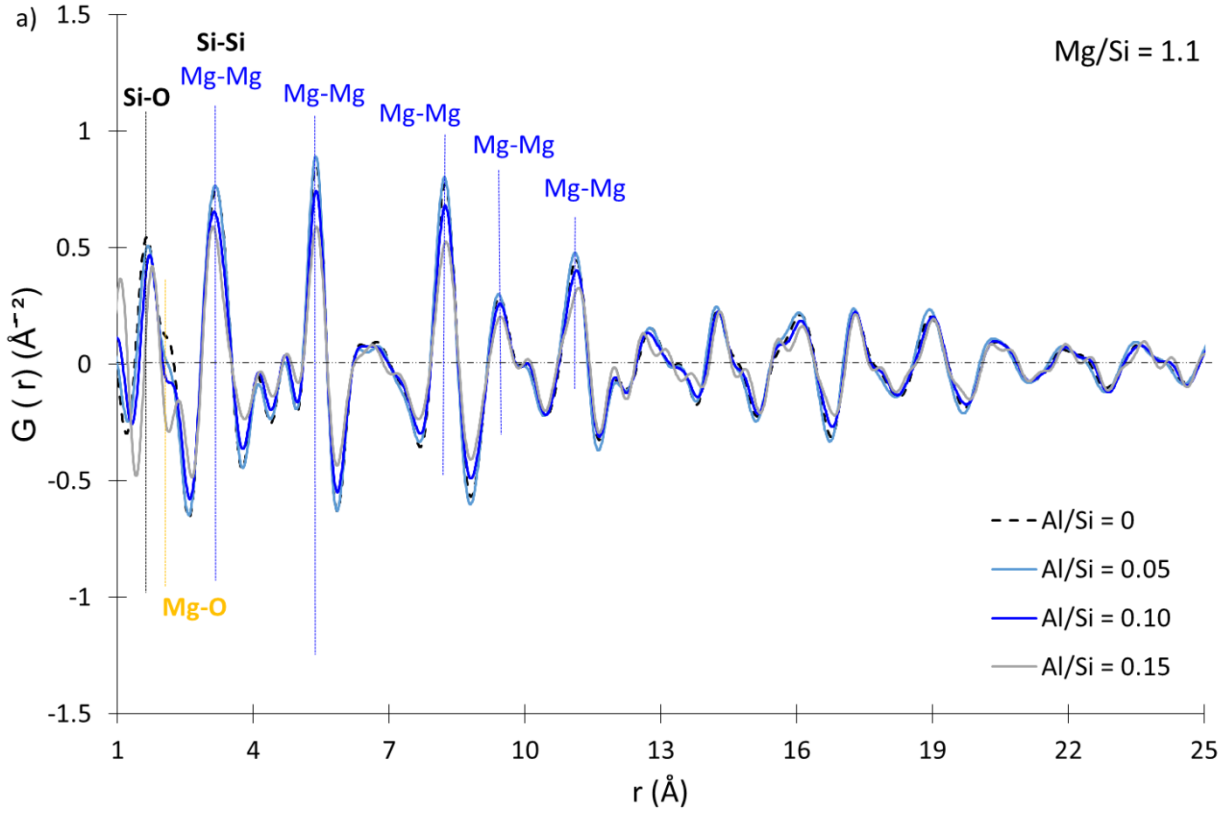

400

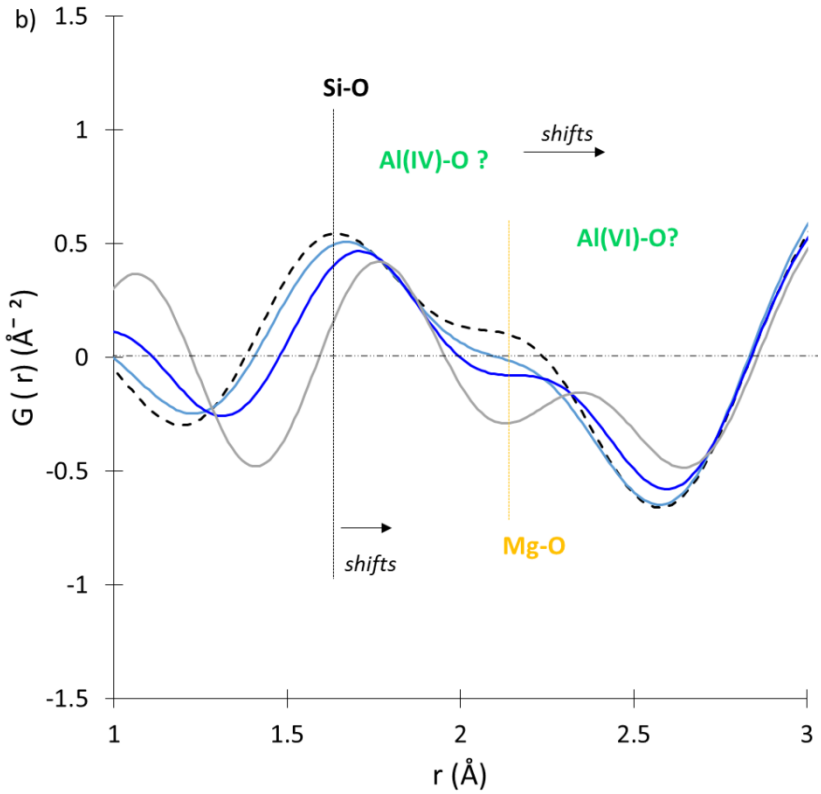

401
402 *Figure 7: Reduced pair distribution function of M-A-S-H samples (Al/Si= 0.05, 0.10, 0.15, 1 year – 50°C) compared to M-*
403 *S-H sample (Al/Si=0).*

The composition of the solutions at equilibrium of the M-A-S-H samples is shown in Table 3. At 20°C a pH value of 9.8 was reached and, silicon and magnesium concentrations of 0.008 mmol/L and 0.15 mmol/L, respectively, were determined in the absence of aluminum. When metakaolin was present, the pH values ranged from 9.8 to 10.0 and the silicon concentrations from 0.01 to 0.02 mmol/L. Higher concentrations (0.3 mmol/L) of silicon were detected in the sample with the highest metakaolin content (Al/Si = 0.2), where the presence of unreacted silica indicated that equilibrium was not yet reached. The magnesium concentrations were between 0.15 and 0.41 mmol/L. Similar results were obtained for the samples equilibrated at 50 and 70°C, confirming that the addition of metakaolin had no significant effect on pH or Mg or Si concentrations. The concentrations of dissolved Al for all samples were close to or below the detection limit of 0.0001 mmol/L, confirming that aluminum released by the dissolution of metakaolin effectively was precipitated in the solid phase.

Saturation indices (SI) with respect to amorphous silica, $Mg(OH)_2$, $Al(OH)_3$ and hydrotalcite ($Mg_4Al_2(OH)_{14}\cdot(H_2O)_3$), M-S-H, montmorillonite, vermiculite, and saponite were calculated from the measured ion concentrations and pH values in the pore solution and summarized in Table 5. A negative saturation index (SI) indicates that the solution is undersaturated and the respective solid should not form or will dissolve if present. In contrast, a positive saturation index means that the solution is oversaturated and the formation of the respective solid is possible. The SI calculated for M-S-H 1.1 sample showed that the solutions at 20°C were largely undersaturated with respect to brucite and amorphous silica in agreement with the absence of these phases. For higher aluminum contents of the M-A-S-H phases, only a slight undersaturation with respect to silica was observed. These solutions were also undersaturated with respect to microcrystalline aluminum hydroxide and hydrotalcite, again in agreement with the absence of these solid phases. All solutions were saturated with respect to M-S-H. The calculations have also shown that the solutions were oversaturated with respect to crystalline magnesium aluminum silicate hydrates

such as saponite and vermiculite, which were used as proxies for M-A-S-H phases in the SI calculations, but undersaturated with respect to montmorillonite, which has a high aluminum and silicon content but contains only small amounts of magnesium. The formation of crystalline saponite or vermiculite, both magnesium alumino-silicate clays, was not observed, although the positive SI may indicate the possible formation of these M-A-S-H phases, which are considered as precursors of such clays.

The determined ion concentrations in the solution (Table 3) were also used to calculate ion activity products (IAP) for three possible aluminum containing M-A-S-H phases with different Mg/Si, based on the solid solution from [13] with extreme Mg/Si ratios equal to 0.75 and 1.5, and with Al/Si equal to 0.2 resulting in log IAP = -15.0 ± 0.4 for $M_{0.75}A_{0.20}SH_{1.50}$, log IAP = -18.2 ± 0.4 for $MA_{0.20}SH_{1.75}$ and log IAP = -24.0 ± 0.4 for $M_{1.50}A_{0.20}SH_{1.80}$. These ion activity products are very similar to the solubility products previously obtained for pure M-S-H phases [13, 22], as shown in Figure 8. For all M-S-H and M-A-S-H samples, the ion activity products decreased strongly when the Mg/Si ratio increased. Moreover, the IAPs of M-A-S-H samples were not significantly influenced by the Al content. The ion activity products corresponding to the formula of crystalline vermiculite ($Mg_{1.09}Al_{0.27}SiO_{5.95}H_{4.91}$) and saponite ($Mg_{0.87}Al_{0.09}SiO_{5.32}H_{4.64}$) were also calculated and compared with the solubility products of crystalline vermiculite and saponite. The solubility products of the crystalline clay minerals (red diamonds in Figure 8) were somewhat lower than those of M-A-S-H of similar compositions, consistent with the observation that M-A-S-H may be a poorly ordered precursor and thus slightly less stable than their crystalline analogues. Note that the data of vermiculite and saponite also show the same trend as M-A-S-H: the solubility decreases with increasing Mg/Si ratio [13, 22, 64] and varies only little with aluminum content.

Table 5: Calculated saturation indices (SI) and ion activity products (IAP) of M-A-S-H phases (2 years, 20°C) calculated from the solution state ion concentrations (Table 3) and the thermodynamic data (Table 2). Solid phases observed experimentally are highlighted in bold.

initial Mg/Si & Al/Si	saturation indices (SI)								log IAP[b]				
	$Mg(OH)_2$	Hydrotal.[a]	$Al(OH)_3$	SiO_2	MSH	Vermiculite	Montmoril.	Saponite	M-A-S-H Mg/Si=0.75	M-A-S-H Mg/Si=1	M-A-S-H Mg/Si=1.5	Vermiculite Mg/Si=1.1	Saponite Mg/Si=0.9
1.1 - 0	-1.6			-2.4	**-0.5**								
1.1 - 0.05	-1.1	-3.3	-1.4	-2.4	**0.5**	7.5	-3.1	6.1	*-15.0*	*-18.0*	-24.2	-19.3	-16.2
1.1 - 0.10	-1.1	-4.0	-1.7	-2.3	**0.6**	7.6	-3.1	6.4	*-14.9*	*-18.0*	-24.2	-19.3	-16.1
1.1 - 0.15	-1.2	-3.8	-1.6	-2.4	**0.4**	7.4	-3.3	6.1	*-15.0*	*-18.1*	-24.2	-19.4	-16.2
1.1 - 0.20[c]	**-1.6**	-5.0	-1.3	**-0.7**	**2.9**	11.3	3.5	10.9					
1.6 - 0	**-0.3**			-3.8	**-0.1**								
1.7 - 0.05	**-0.1**	-0.5	-2.1	-3.6	**0.6**	6.8	-8.5	4.8	-15.5	*-18.3*	*-23.9*	-19.6	-16.5
1.7 - 0.10	**-0.1**	-0.8	-2.1	-3.4	**0.8**	7.1	-7.8	5.2	-15.4	*-18.2*	*-23.9*	-19.5	-16.4
1.7 - 0.15	**-0.4**	-1.7	-1.9	-3.3	**0.4**	6.7	-7.2	4.9	-15.4	*-18.3*	*-24.1*	-19.6	-16.5
1.7 - 0.20[c]	**-0.8**	**-2.4**	**-1.6**	-1.9	**1.9**	10.1	-1.1	9.0					
Average IAP									-15.0		-24.0		

[a] $Mg_4Al_2(OH)_{14}.(H_2O)_3$

[b] IAP $(M_{0.75}A_{0.2}SH_{1.5}) = {}^{0.75}\{AlO_2^-\}^{0.2}\{SiO_2^0\}\{OH^-\}^{1.3}\{H_2O\}^{1.5}$;
IAP $(M_1A_{0.2}SH_{1.75}) = \{Mg^{2+}\}\{AlO_2^-\}^{0.2}\{SiO_2^0\}\{OH^-\}^{1.8}\{H_2O\}^{1.75}$;
IAP $(M_{1.5}A_{0.2}SH_{1.8}) = \{Mg^{2+}\}^{1.5}\{AlO_2^-\}^{0.2}\{SiO_2^0\}\{OH^-\}^{2.8}\{H_2O\}^{1.8}$;
IAP (Vermiculite) $= \{Mg^{2+}\}^{0.87}\{AlO_2^-\}^{0.09}\{SiO_2^0\}\{OH^-\}^{1.64}\{H_2O\}^{1.5}$;
IAP (Saponite) $= \{Mg^{2+}\}^{1.09}\{AlO_2^-\}^{0.27}\{SiO_2^0\}\{OH^-\}^{1.91}\{H_2O\}^{1.5}$. {} indicates activity

[c] Not considered for the average calculated value since samples are not in equilibrium

italic = data considered for the average calculated IAP.

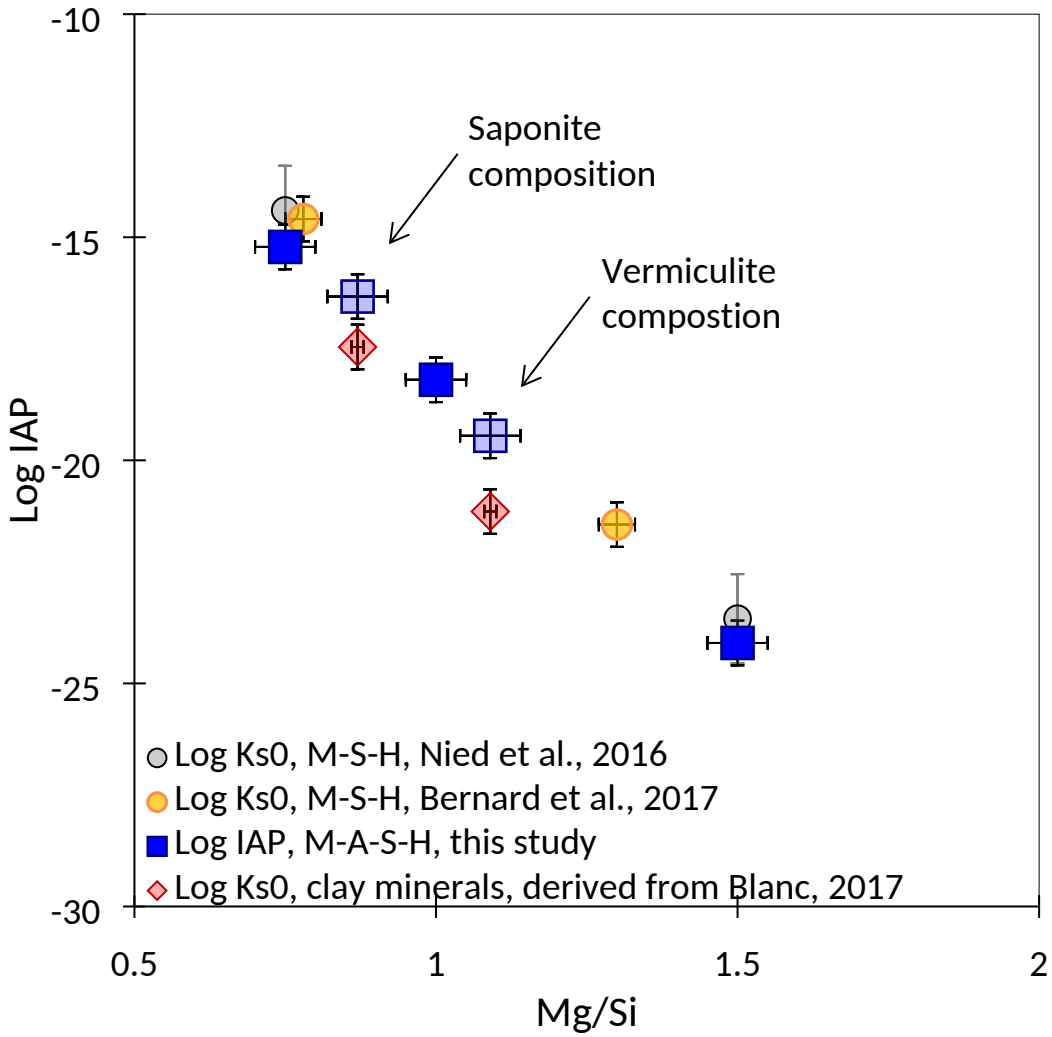

Figure 8: Calculated ion activity products of magnesium alumino-silicate hydrate (squares) at room temperature as a function of the total Mg/Si, compared to the solubility products of pure M-S-H (Nied et al. ; Bernard et al. [13, 22] (circles) and to the solubility products of vermiculite and saponite (diamonds; taken from Blanc.; (Thermoddem database) [40]). Full squares correspond to M-A-S-H with Al/Si=0.20, while the lighter squares and the diamonds correspond to different Al/Si: Mg/Si=0.9 & Al/Si=0.1 for saponite and Mg/Si=1.1 & Al/Si=0.3 for vermiculite.

The cation exchange capacity (CEC) measures the amount of exchangeable cations present either in the interlayer of particles (as in clays) and/or on the surface (in the Stern and diffuse layers) of nano-sized particles. The M-A-S-H samples had a positive CEC, meaning that their surface area was negatively charged, similar to phyllosilicates. Moreover, the CEC values of M-A-S-H were similar to that of pure M-S-H of around 38-40 ± 4 meq/100g (see black dots in Figure 9 and Table 6). A small effect of aluminum

in M-A-S-H compared to M-S-H on the charge is to be expected, since only a small excess of octahedrally coordinated aluminium is present (Al(VI)/Al(IV) ratios ≈1.5 calculated from the ^{27}Al NMR data). This slight surplus of octahedral aluminum in the octahedral MgO layer may reduce the negative charge lowering the CEC.

The total of the cations released by the cobalt(III) substitution (bars in Figure 9) agreed well with the CEC measured by colorimetry (dots). As for pure M-S-H [15], the content of exchangeable cations was low (equal to 0.02 – 0.03 Mg/Si) and the cations were mainly magnesium plus a small amount of alkalis (lithium, sodium, and potassium present as impurities in metakaolin). Aluminum was not detected as an exchangeable cation since it occurs mainly as $Al(OH)_4^-$ at pH values above 7 [65]. The absence of aluminum at the cation exchange sites indicates that aluminum was only incorporated in the tetra- and octahedral sheets of the magnesium silicate phase, but not at exchangeable sites on the surface.

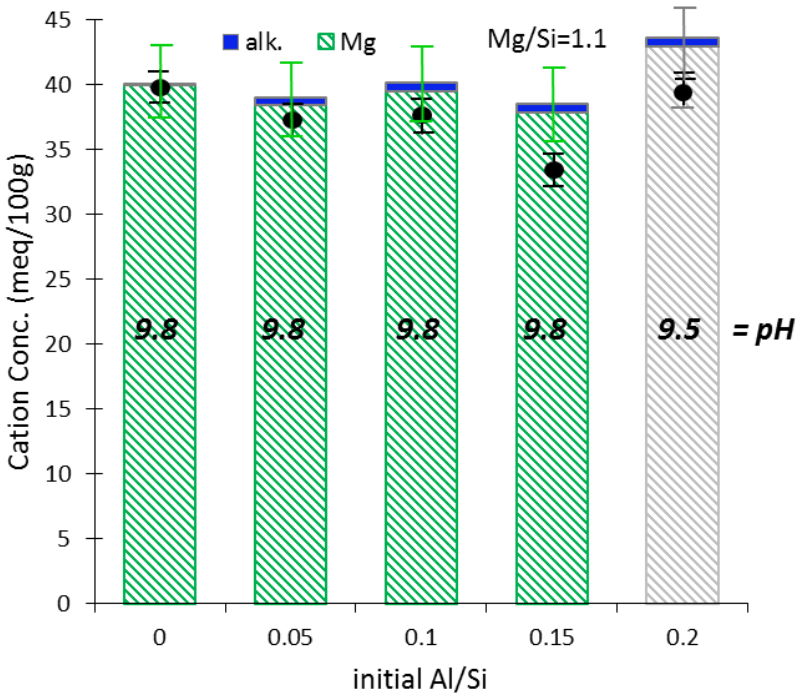

Figure 9: Concentrations of the cations sorbed on M-A-S-H 1.1 measured by the cobalt hexamine method as a function of the initial Al/Si. The cation exchange capacity (CEC) measurements by colorimetry (black dots) have been added for comparison. Sample with Al/Si=0.2 not at equilibrium is shown in grey. alk. = Li, Na or K impurities from metakaolin starting material.

Table 6: CEC data for the M-A-S-H samples..

M-A-S-H					
Mg/Si	1.1	1.1	1.1	1.1	1.1
Al/Si	0	0.05	0.1	0.15	0.2
Measured data (meq/100g)					
total of cations released by Co(III) (measured by IC). Measurement error ± 4	*40.1*	*39.1*	*40.2*	*38.6*	*43.7*
data from the Co(III) sorption method (measured by colorimetry). Error ± 2	39.9	37.1	37.7	33.2	39.1
Mg_{exch}/Si	0.028	0.027	0.028	0.027	-
Mg/Si	1.6	1.7	1.7	1.7	1.7
Al/Si	0	0.05	0.1	0.15	0.2
Measured data (meq/100g)					
*total of cations released by Co(III) (measured by IC). Measurement error ± 4**	*47.3*	*35.5*	*36.6*	*36.2*	*36.4*
data from the Co(III) sorption method (measured by colorimetry). Error ± 2	35.9	31.1	30.9	31.0	35.3
Corrected for dilution by brucite					
data from the Co(III) sorption method (measured by colorimetry). Error ± 2.4	43.8	38.8	38.6	38.7	44.2
Mg_{exch}/Si	0.035	0.031	0.031	0.031	-

**: not used as it might have a brucite dissolution in those samples*

Zeta potential measurements on M-S-H and M-A-S-H 1.1 particles were plotted versus the initial Al/Si (Figure 10a). As for M-S-H [15], the zeta potential of M-A-S-H was negative, which corresponds to the negative surface charge observed by CEC. Note that the pH was almost constant in the samples and was not responsible for any deviation in the zeta potential. The zeta potential of the M-A-S-H samples was with -20 ± 2 mV (Figure 10) slightly less negative than that of pure M-S-H 1.1 (approx.-25 mV), with the exception of the sample with the highest aluminum addition (Al/Si = 0.2) of -25 ±3 mV, where amorphous silica was still present. This more negative zeta potential value at Al/Si = 0.2 can be explained by the very negative zeta potential of amorphous silica (< - 40 ± 4 mV) at this pH [15]. The slightly less negative zeta potential of about -20 ± 2 mV for M-A-S-H is consistent with slightly lower CEC and the ^{27}Al NMR results, which showed an only slightly higher Al(VI)/Al(IV) ratio.

In addition, the increasing magnesium concentration from 0.15 mmol/L (pure M-S-H) to 0.41 mmol/L (M-A-S-H with Al/Si = 0.1) may also contribute to less negative zeta potentials (Figure 10b) as higher magnesium contents in the diffuse and/or Stern layer near the M-A-S-H surface dcrease the measured zeta potential [15]. The zeta potential is therefore strongly related to the concentration of dissolved magnesium: the higher the magnesium concentration in solution, the less negative is the zeta potential of M-(A-)S-H, which shows the presence of dissolved magnesium in the Stern and diffuse layer, i.e. very close to the silicate surface. Similar observations have been reported for calcium silicate hydrates (C-S-H), where increased Ca^{2+} concentrations augmented the zeta potential of C-S-H [66].

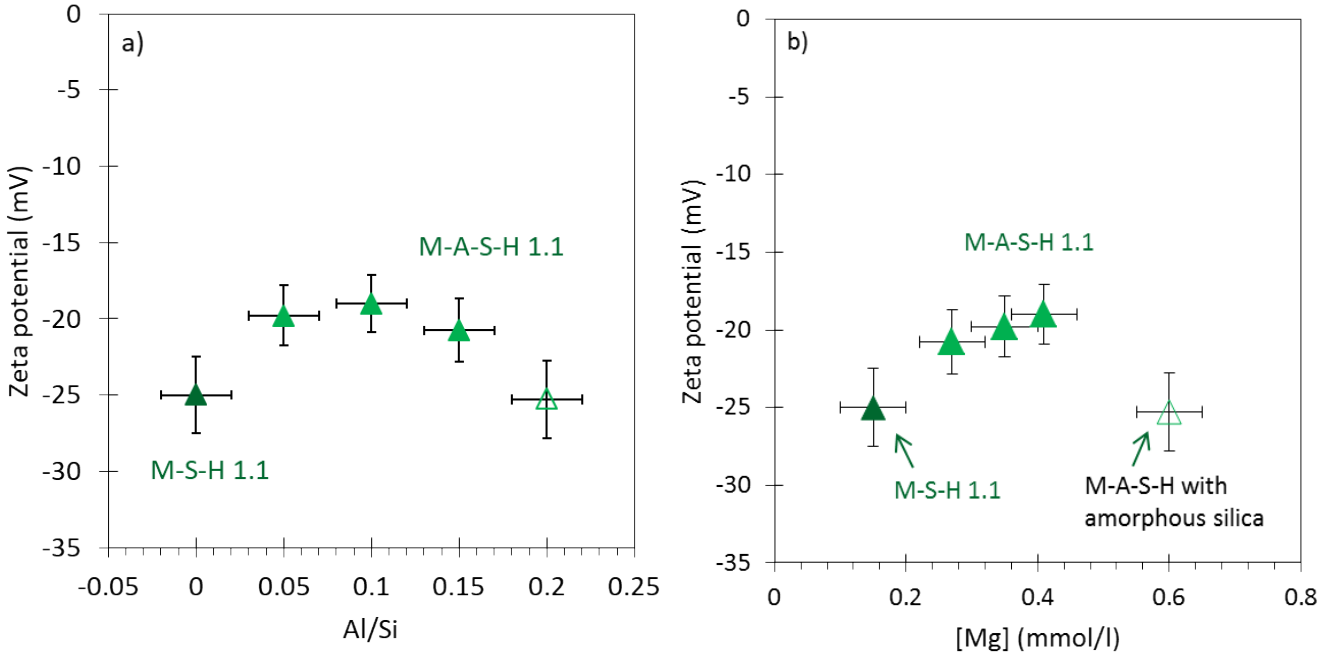

Figure 10: Measured zeta potentials as a function of a) the Al/Si in the M-A-S-H samples (2 years, 20°C) Mg/Si=1.1, b) of dissolved magnesium; M-S-H 1.1 references from [15].

3.2. M-A-S-H 1.7

The aluminum uptake was also studied at high Mg/Si ratios (1.6-1.7). Under these conditions, brucite precipitates in addition to M(-A)-S-H phases, as shown by TG analysis and XRD (Figure 3). Regardless of the quantity of metakaolin originally added, about 20 wt.% of brucite is precipitated in the samples

cured at 20, 50 and 70°C (Table 3), indicating a maximum Mg/Si ratio of 1.4 in the M-A-S-H solid phases at all temperatures, consistent with previous observations of pure M-S-H phases [13, 22]. In the M-A-S-H 1.7 sample with the highest Al/Si ratio (0.20), after 1 year of curing at 20°C, small amounts of unreacted amorphous silica were still detected by ^{29}Si MAS NMR, but silica was fully depleted after 2 years (Table 3). Semi-amorphous aluminum hydroxide, hydrotalcite were also detected by TGA for Al/Si = 0.2 at both characterization times (Supplementary Information, Figure S1 and Table 3). The presence of these phases, which were not observed in the previous syntheses performed at lower Mg/Si ratio (1.1), may indicate that the uptake of aluminum by M-S-H is limited at high Mg/Si ratios as observed by TEM in Figure 5.

The ^{27}Al MAS NMR spectra of the M-A-S-H samples with Mg/Si = 1.7 did also not vary with the amount of metakaolin added (Figure 6c, Table 4). Aluminum was again observed in two different environments; about 75% were six-fold coordinated (Al[VI]) and 25% four-fold coordinated (Al[IV]). Again, it can be assumed that the Al(IV) and a part of the Al(VI) correspond to the incorporation of aluminum in the tetrahedral and octahedral layers of the M-S-H. The higher fraction of six fold coordinated aluminum, which replaces magnesium, could reduce the negative surface charge. In the sample with Al/Si = 0.2 and a curing temperature of 20°C, small amounts of hydrotalcite and micro crystalline aluminum hydroxide contribute also to the NMR signal. Additionally, at lower aluminum content, micro crystalline aluminum hydroxide may actually be present in small quantities (below the detection limit of TGA and XRD) in the all series, which would decrease the effective Al/Si in M-A-S-H. The TEM data confirm this hypothesis since the Al/Si ratio in M-A-S-H 1.1 was measured at 0.06 instead of 0.10.

The increasing fraction of Al(VI) in M-A-S-H 1.7 samples, as compared to M-A-S-H 1.1 samples (see Table 4), is consistent with the structure of these two phases: increasing the Mg/Si ratio gives more possibilities for substitutions in the octahedral layer than in the tetrahedral layer of M-S-H.

538 The aqueous phase of pure M-S-H 1.6 sample equilibrated at 20°C had a pH of ~10.5, and magnesium
539 and silicon concentrations of 0.12 mmol/l and 0.001 mmol/l, respectively (Table 3). These data are in
540 good agreement with previous characterizations performed on M-S-H samples with high Mg/Si ratio,
541 where brucite was also present [22, 24]. The aqueous phase of M-A-S-H 1.7 samples had a composition
542 very close to that of M-S-H 1.6. As observed at low Mg/Si ratio, the addition of metakaolin did not
543 significantly change the concentrations of dissolved species at equilibrium.

544 The saturation indices (SI, Table 5) showed that the solutions stored at 20°C were undersaturated with
545 respect to amorphous silica. The undersaturation was smaller for the sample with the highest Al/Si ratio,
546 as previously observed for the M-A-S-H 1.1 series. The solutions were also undersaturated with respect
547 to brucite, which was however detected in the solid phase. This result can be explained by a kinetic
548 hindrance of brucite dissolution in the presence of silicon as reported in [22]. As for the M-A-S-H 1.1
549 series, the solutions were undersaturated with respect to montmorillonite, oversaturated with respect to
550 saponite and vermiculite, and close to saturation with respect to M-S-H. The saturation indices tended to
551 increase slightly in the presence of aluminum. Most of the aluminum concentrations were close to the
552 detection limit and the solutions were undersaturated with respect to microcrystalline aluminum hydroxide
553 and hydrotalcite, which is consistent with their non-detection by XRD and TG analysis (except at Al/Si =
554 0.2, where hydrotalcite was probably present, see Table 3).

555 The CEC obtained for the M-A-S-H 1.7 samples were compared to those of M-S-H 1.6 (which contained
556 85% wt of M-S-H and 15%wt of brucite) with a pH of 10.5 (Table 6). In all cases, magnesium and sodium
557 were the only exchangeable cations identified by CEC, indicating again that aluminum was present in the
558 M-S-H layers as a M-(A-)S-H phase or in other solid phases.

559 Previous studies using M-S-H [20] and the M-A-S-H 1.1 samples (see Table 6 and Figure 9) have shown
560 in general a good consistency between the two sets of CEC data determined by different analytical
561 methods. Both types of samples contained pure phases without hydroxide minerals and had pH lower than
562 10.5. However, in the case of M-S-H 1.6 sample, the CEC based on the total of cations released by the
563 cobalt(III) replacement (CEC measured by IC, see "measured" data in Table 6) was higher than the total
564 CEC measured using the complex binding of Co(III) (CEC colorimetry, cf. raw data in Table 6). This
565 deviation can be explained by the dissolution of solid brucite in the rather acidic cobalt hexamine
566 trichloride solution used for the CEC determination, resulting in an overestimation of the magnesium
567 concentration. Therefore, the results based on the measured Mg and Na concentration measured by IC
568 overestimated CEC, while the total CEC measured using the complex binding of Co(III) mirrored the
569 CEC more closely.

570 Thus the further discussion focusses on the CEC measured by Co(III) complexation (CEC colorimetry).
571 Both samples M-S-H 1.6 and M-A-S-H 1.7 contained additional amounts of brucite of ~18%wt and
572 20%wt, respectively. This means that the CECs determined by colorimetry were lower than the true CECs
573 due to dilution of M-(A-)S-H by brucite. The correction for this dilution effect resulted in CEC values of
574 ~44 meq/100g for M-S-H 1.6, which are only slightly higher than the CEC of M-S-H 1.1 (~40 meq/100g;
575 Table 6) or M-S-H 1.2 (~42 meq/100g) [15]. The values for the M-(A-)S-H samples with Al/Si = 0.05,
576 0.1 and 0.15, however, were with ~38 meq/100g slightly lower, consistent with the higher content of Al
577 in octahedral sites than tetrahedral sites (Al(VI)/Al(IV) ratios of ~ 3; Table 4), which partially compensates
578 the negative surface charge. In the sample Al/Si= 0.2 with unreacted silica and brucite no decrease of the
579 CEC was observed. Thus, the measured CEC data become in tendency lower in the presence of Al, but
580 the difference are relatively small considering the error of the data. This only very limited reduction of the
581 cation exchange capacity (from 0.035 Mg/Si to 0.031 Mg/Si) could indicate that the incorporation of

aluminum in the octahedral sheet is at least partially compensated by the presence of additional vacancies in the octahedral magnesium oxide sheet, as in the case of di-octahedral silicates such as montmorillonite [17].

A slightly less negative zeta potential (-18 ± 2 mV) was determined for samples containing aluminum, as compared with M-S-H 1.6 (-23 mV) (Figure 12). As discussed above, the concentration of magnesium (between 0.1 and 0.2 mmol/L) and the pH values all remained constant regardless of the initial content of metakaolin. Thus, the less negative zeta potential measured for M-A-S-H 1.7 could be related to the presence of a slightly more brucite having a positive zeta potential [67] in these samples, and possibly to the less negative surface charge induced by the higher content of aluminum in the octahedral sites since the corrected CEC values increased also slightly in presence of aluminum.

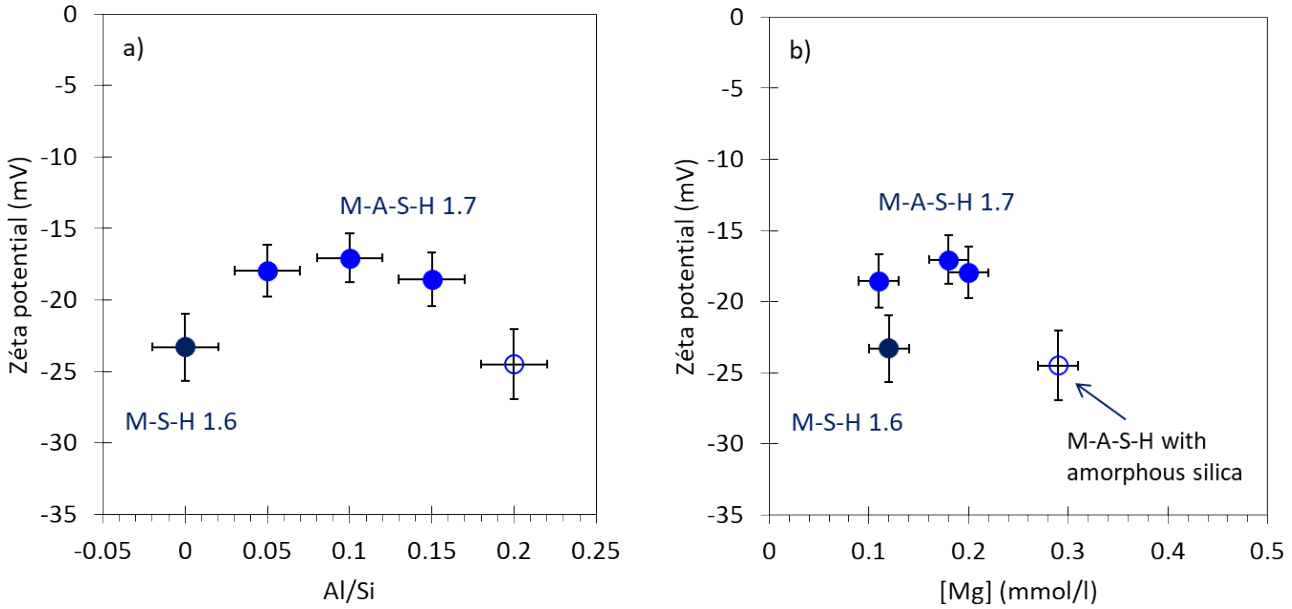

Figure 11: Measured zeta potentials a) as a function of pH in the M-A-S-H samples (2 years, 20°C) Mg/Si=1.7 and b) as a function of the measured magnesium concentrations.

At high Mg/Si ratios, ^{27}Al MAS NMR data showed the preferred incorporation of aluminum into octahedral sites, which could lead to a lower negative surface charge as determined by CEC and zeta potential determinations. The CEC data showed that magnesium was the main exchangeable cation in the M-A-S-H phases as for M-S-H, while aluminum was not observed among the exchangeable cations. This is consistent with the very low aluminum concentration beyond the detection limit of 0.0001 mmol/L in solution, and with its speciation, $Al(OH)_4^-$ being the dominant species at pH 10.

4. Conclusions

This work aimed at investigating the aluminum incorporation into magnesium silicate hydrate. Up to approx. 0.15-0.18 aluminum per silica (for an addition of Al/Si=0.2) were incorporated in M-A-S-H at high silica content. The maximum uptake of aluminum by M-S-H still needs to be determined. ^{29}Si and ^{27}Al MAS NMR data, thermogravimetric analysis (TGA), and X-ray diffraction (XRD) showed that M-A-S-H phases were formed with the same silicate polymerization process as pure M-S-H. In batch experiments we observed the same slow formation for M-S-H and M-A-S-H phases: the initially formed excess of brucite subsequently slowly reacted with amorphous silica to yield M-(A-)S-H. The PDF analysis showed that the M-A-S-H samples had a limited coherence length and pointed towards an incorporation in both the silica and magnesium oxide layers.

^{29}Si and ^{27}Al MAS NMR data confirmed that aluminum was incorporated into both the octahedral and tetrahedral sheets. At Mg/Si = 1.1, aluminum was distributed between octahedral (60%) and tetrahedral (40%) positions, independent on the amount of Al present. At higher Mg to Si ratio (Mg/Si = 1.7), the fraction of aluminum in the octahedral magnesium hydroxide layer in M-A-S-H increased to ca. 75%, again independent of the amount of aluminum added. This increase of aluminum in the magnesium oxide sites led only to a slight reduction of the negative surface charge and of the cation exchange capacity,

indicating that the incorporation of aluminum in the octahedral sheet could be partially compensated by the presence of additional vacancies in octahedral magnesium oxide sheet, as for di-octahedral silicates such as montmorillonite. The CEC measurements showed that presence of some magnesium at the cation exchange sites (~ 0.03 Mg/Si), but not of aluminum.

Similar solution and solid compositions were observed at 50 and/or 70°C, indicating little influence of temperature on the stability of M-A-S-H as observed for M-S-H [22]. Our study provides data for aqueous and solid compositions that could serve as a basis to extend thermodynamic models previously developed for M-S-H [13, 20, 22] to M-A-S-H. Such models will be necessary to describe the changes at the interface between a cement paste and a magnesium-containing environment such as clays.

Acknowledgements

The authors would like to thank Alexandre Dauzères and the French Institute of Radiation Protection and Nuclear Safety for the funding of Ellina Bernard's Ph.D.; Jorgen Skibsted is acknowledged for helpful discussions, Christophe Chlique and Nicolas Courtois from CEA for their help concerning the PDF analysis, and Remi Chassagnon for the TEM analyses. The NMR hardware was partially granted by the Swiss National Science Foundation (SNSF, grant no. 206021_150638/1).

Supplementary data

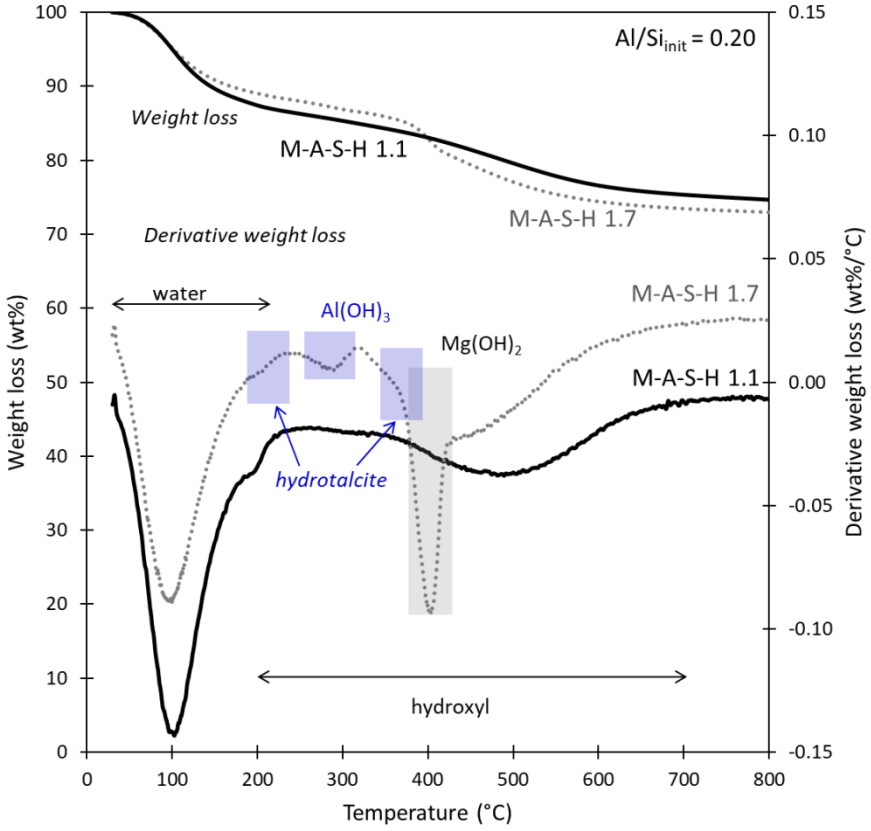

Figure S1: TGA data with assignments of chemical species of M-A-S-H samples with initial Mg/Si=1.1 and 1.7 and Al/Si = 0.2.

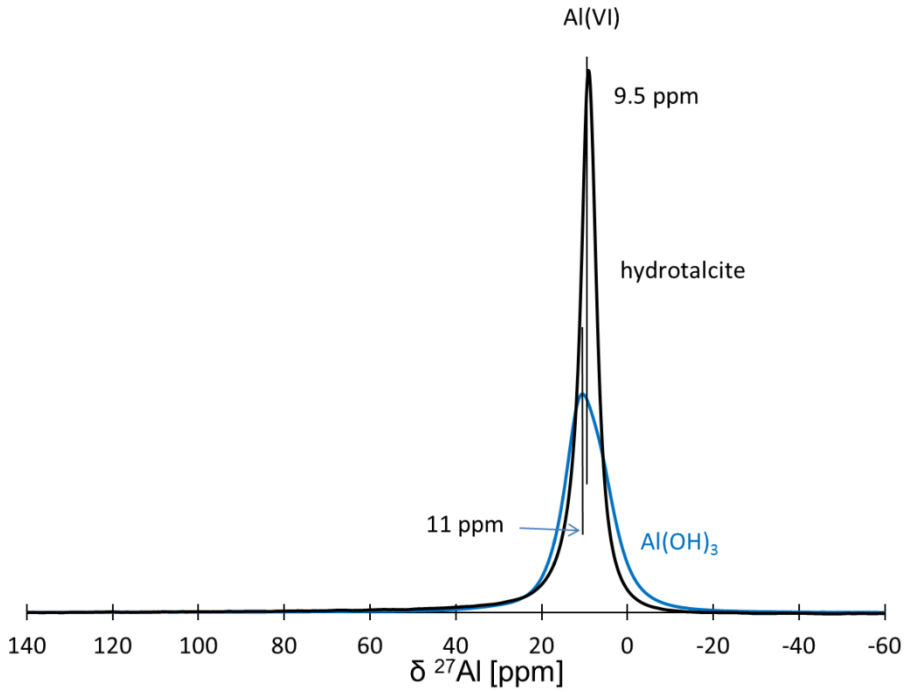

Figure S2: ^{27}Al MAS NMR spectra of synthesized hydrotalcite and synthesized poorly ordered Al(OH)$_3$.

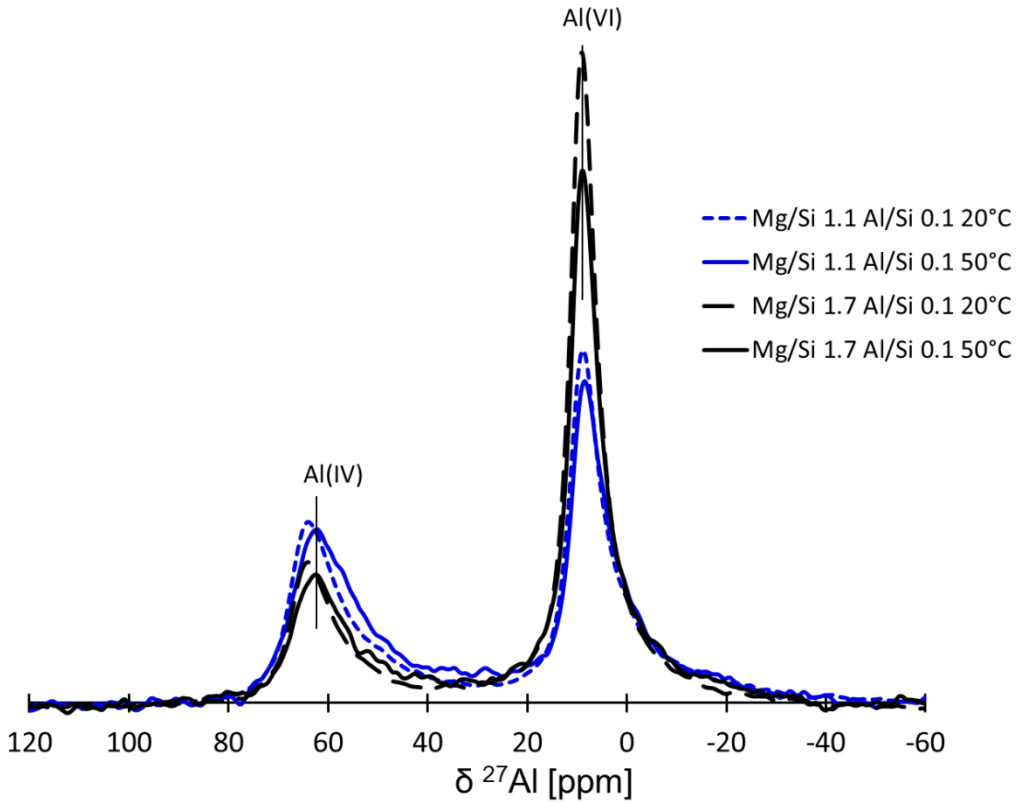

Figure S3: ^{27}Al MAS NMR spectra of M-A-S-H phases Mg/Si=1.1 and 1.7 at constant Al/Si=0.10: comparison between the samples cured during 1 year at 50°C and the samples cured during 2 years at 20°C.

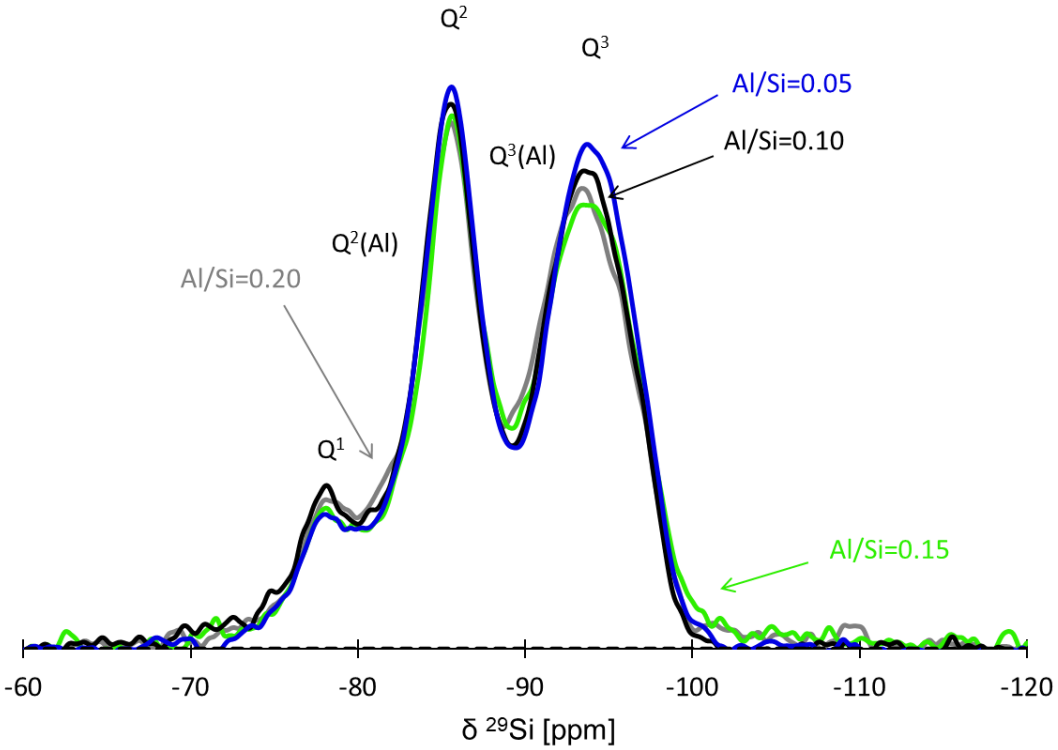

Figure S4: ^{29}Si MAS NMR spectra with assignments of Q^n environments of the M-A-S-H samples, Mg/Si=1.7 and Al/Si=0.05-0.20 (all samples cured for 1 year at 50°C).

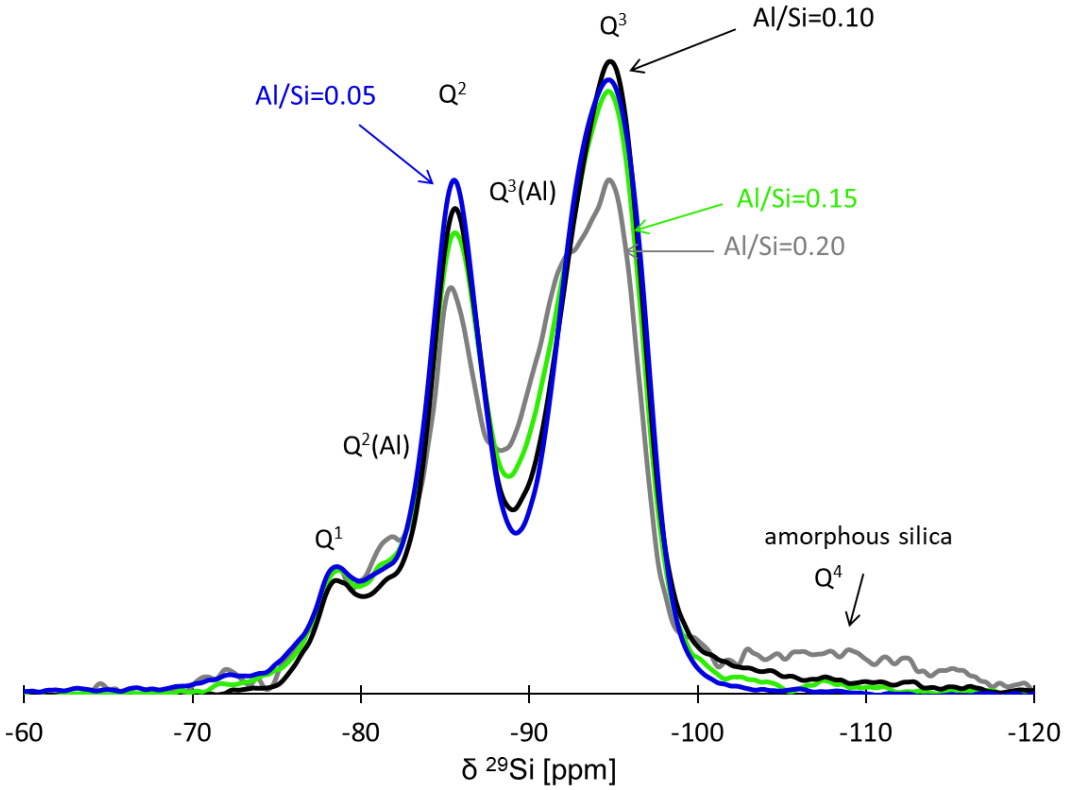

Figure S5: ^{29}Si MAS NMR spectra with assignments of Q^n environments of the M-A-S-H samples, Mg/Si=1.1 and Al/Si=0.05-0.20 (all samples cured for 2 years at 20°C).

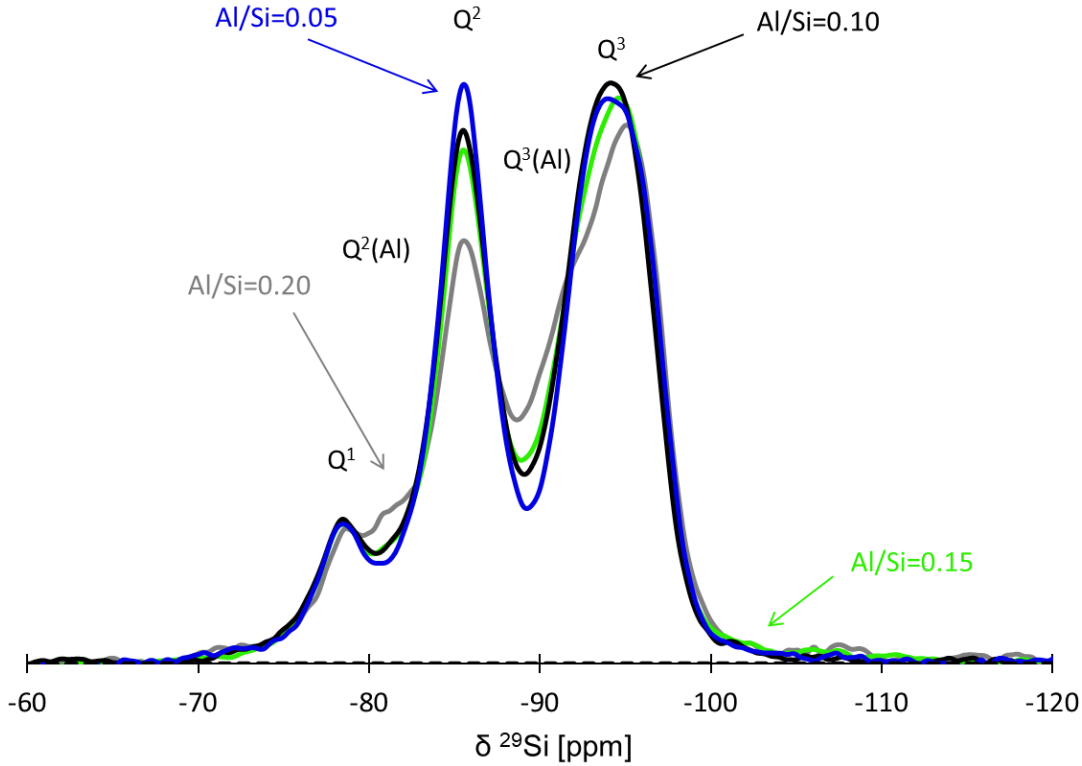

Figure S6: ^{29}Si MAS NMR spectra with assignments of Q^n environments of the M-A-S-H samples, Mg/Si=1.7 and Al/Si=0.05-0.20 (all samples cured for 2 years at 20°C).

References:

[1] A. Jenni, U. Mäder, C. Lerouge, S. Gaboreau, B. Schwyn, In situ interaction between different concretes and Opalinus clay, Physics and Chemistry of the Earth, Parts A/B/C, 70 (2014) 71-83.

[2] A. Dauzères, G. Achiedo, D. Nied, E. Bernard, S. Alahrache, B. Lothenbach, Magnesium perturbation in low-pH concretes placed in clayey environment - solid characterizations and modeling, Cement and Concrete Research, 79 (2016) 137-150.

[3] J.L. Garcia Calvo, A. Hidalgo, C. Alonso, L. Fernández Luco, Development of low-pH cementitious materials for HLRW repositories: Resistance against ground waters aggression, Cement and Concrete Research, 40 (2010) 1290-1297.

[4] C. Lerouge, S. Gaboreau, S. Grangeon, F. Claret, F. Warmont, A. Jenni, V. Cloet, U. Mäder, In situ interactions between Opalinus Clay and Low Alkali Concrete, Physics and Chemistry of the Earth, Parts A/B/C, 99 (2017) 3-21.

[5] U. Mäder, A. Jenni, C. Lerouge, S. Gaboreau, S. Miyoshi, Y. Kimura, V. Cloet, M. Fukaya, F. Claret, T. Otake, M. Shibata, B. Lothenbach, 5-year chemico-physical evolution of concrete-claystone interfaces, Swiss Journal of Geosciences, 110 (2017) 307-327.

[6] D. Bonen, M.D. Cohen, Magnesium sulfate attack on portland cement paste—II. Chemical and mineralogical analyses, Cement and Concrete Research, 22 (1992) 707-718.

[7] M. Santhanam, M.D. Cohen, J. Olek, Mechanism of sulfate attack: a fresh look: part 1: summary of experimental results, Cement and concrete research, 32 (2002) 915-921.

[8] K. De Weerdt, H. Justnes, The effect of sea water on the phase assemblage of hydrated cement paste, Cement and Concrete Composites, 55 (2015) 215-222.

[9] E. Bernard, A. Dauzères, B. Lothenbach, Magnesium and calcium silicate hydrates, Part II: Mg-exchange at the interface “low-pH” cement and magnesium environment studied in a C-S-H and M-S-H model system, Applied Geochemistry, 89 (2018) 210-218.

[10] M.B. Haha, B. Lothenbach, G. Le Saout, F. Winnefeld, Influence of slag chemistry on the hydration of alkali-activated blast-furnace slag—Part I: Effect of MgO, Cement and Concrete Research, 41 (2011) 955-963.

[11] A. Machner, M. Zajac, M.B. Haha, K.O. Kjellsen, M.R. Geiker, K. De Weerdt, Limitations of the hydrotalcite formation in Portland composite cement pastes containing dolomite and metakaolin, Cement and Concrete Research, (2018).

[12] S.A. Bernal, R. San Nicolas, R.J. Myers, R.M. de Gutiérrez, F. Puertas, J.S. van Deventer, J.L. Provis, MgO content of slag controls phase evolution and structural changes induced by accelerated carbonation in alkali-activated binders, Cement and Concrete Research, 57 (2014) 33-43.

[13] D. Nied, K. Enemark-Rasmussen, E. L'Hopital, J. Skibsted, B. Lothenbach, Properties of magnesium silicate hydrates (MSH), Cement and Concrete Research, 79 (2016) 323-332.

[14] C. Roosz, S. Grangeon, P. Blanc, V. Montouillout, B. Lothenbach, P. Henocq, E. Giffaut, P. Vieillard, S. Gaboreau, Crystal structure of magnesium silicate hydrates (MSH): The relation with 2: 1 Mg–Si phyllosilicates, Cement and Concrete Research, 73 (2015) 228-237.

[15] E. Bernard, B. Lothenbach, C. Chlique, M. Wyrzykowski, A. Dauzères, I. Pochard, C. Cau-Dit-Coumes, Characterization of magnesium silicate hydrate (M-S-H), Cement and Concrete Research, 116 (2019) 309-330.

[16] F. Bergaya, G. Lagaly, General introduction: clays, clay minerals, and clay science, Developments in clay science, 1 (2006) 1-18.

[17] M.F. Brigatti, E. Galan, B. Theng, Structure and mineralogy of clay minerals, Developments in clay science, Elsevier2013, pp. 21-81.

[18] R.E. Grim, Clay mineralogy, (1968).
[19] I. Odom, Smectite clay minerals: properties and uses, Philosophical Transactions of the Royal Society of London A: Mathematical, Physical and Engineering Sciences, 311 (1984) 391-409.
[20] E. Bernard, B. Lothenbach, C. Cau-Dit-Coumes, C. Chlique, A. Dauzères, I. Pochard, Magnesium and calcium silicate hydrates, Part I: Investigation of the possible magnesium incorporation in calcium silicate hydrate (C-S-H) and of the calcium in magnesium silicate hydrate (M-S-H), Applied Geochemistry, 89 (2018) 229-242.
[21] E. Bernard, B. Lothenbach, I. Pochard, C. Cau-dit-Coumes, Alkali binding by magnesium silicate hydrates, Journal of the American Ceramic Society, , 00 (2019) 1–15.
[22] E. Bernard, B. Lothenbach, D. Rentsch, I. Pochard, A. Dauzères, Formation of magnesium silicate hydrates (M-S-H), Physics and Chemistry of the Earth, Parts A/B/C, 99 (2017) 142-157.
[23] E. L'Hôpital, B. Lothenbach, G. Le Saout, D. Kulik, K. Scrivener, Incorporation of aluminium in calcium-silicate-hydrates, Cement and Concrete Research, 75 (2015) 91-103.
[24] E. Bernard, B. Lothenbach, F. Le Goff, I. Pochard, A. Dauzères, Effect of magnesium on calcium silicate hydrate (C-S-H), Cement and Concrete Research, 97 (2017) 61-72.
[25] C. Meral, C. Benmore, P.J. Monteiro, The study of disorder and nanocrystallinity in C–S–H, supplementary cementitious materials and geopolymers using pair distribution function analysis, Cement and Concrete Research, 41 (2011) 696-710.
[26] A. Cuesta, R.U. Ichikawa, D. Londono-Zuluaga, G. Angeles, I. Santacruz, X. Turrillas, M.A. Aranda, Aluminum hydroxide gel characterization within a calcium aluminate cement paste by combined Pair Distribution Function and Rietveld analyses, Cement and Concrete Research, 96 (2017) 1-12.
[27] C.E. White, Effects of temperature on the atomic structure of synthetic calcium–silicate–deuterate gels: A neutron pair distribution function investigation, Cement and Concrete Research, 79 (2016) 93-100.
[28] T. Egami, S.J.L. Billinge, Chapter 3. The method of total scattering and atomic pair distribution function analysis, Pergamon Materials Series2003.
[29] P. Juhás, T. Davis, C.L. Farrow, S.J. Billinge, PDFgetX3: a rapid and highly automatable program for processing powder diffraction data into total scattering pair distribution functions, Journal of Applied Crystallography, 46 (2013) 560-566.
[30] N. Cusack, The Physics of Structurally Disordered Matter Hilger, Bristol, UK, (1987) 23.
[31] E. Lorch, Neutron diffraction by germania, silica and radiation-damaged silica glasses, Journal of Physics C: Solid State Physics, 2 (1969) 229.
[32] W.J. Malfait, W.E. Halter, R. Verel, 29Si NMR spectroscopy of silica glass: T1 relaxation and constraints on the Si–O–Si bond angle distribution, Chemical Geology, 256 (2008) 269-277.
[33] D. Massiot, F. Fayon, M. Capron, I. King, S. Le Calvé, B. Alonso, J.O. Durand, B. Bujoli, Z. Gan, G. Hoatson, Modelling one ‐ and two ‐ dimensional solid ‐ state NMR spectra, Magnetic Resonance in Chemistry, 40 (2002) 70-76.
[34] D.R. Neuville, L. Cormier, D. Massiot, Al environment in tectosilicate and peraluminous glasses: A ^{27}Al MQ-MAS NMR, Raman, and XANES investigation, Geochimica et Cosmochimica Acta, 68 (2004) 5071-5079.
[35] M. James, R.J. Hunter, R.W. O'Brien, Effect of particle size distribution and aggregation on electroacoustic measurements of. zeta. potential, Langmuir, 8 (1992) 420-423.
[36] D. Kulik, T. Wagner, S.V. Dmytrieva, G. Kosakowski, F. Hingerl, K.V. Chudnenko, U. Berner, GEM-Selektor geochemical modeling package: revised algorithm and GEMS3K numerical kernel for coupled simulation codes, Computational Geochemistry, 17 (2013) 1-24.

[37] T. Thoenen, W. Hummel, U. Berner, E. Curti, The PSI/Nagra Chemical Thermodynamic Database 12/07, PSI report 14-04, Villigen PSI, Switzerland, (2014).
[38] R.J. Myers, B. Lothenbach, S.A. Bernal, J.L. Provis, Thermodynamic modelling of alkali-activated slag cements, Applied Geochemistry, 61 (2015) 233-247.
[39] B. Lothenbach, E. Bernard, U. Mäder, Zeolite formation in the presence of cement hydrates and albite, Physics and Chemistry of the Earth, Parts A/B/C, 99 (2017) 77-94.
[40] P. Blanc, Thermoddem : Update for the 2017 version., Report BRGM/RP-66811-FR, (2017).
[41] B. Lothenbach, D.A. Kulik, T. Matschei, M. Balonis, L. Baquerizo, B. Dilnesa, G.D. Miron, R.J. Myers, Cemdata18: A chemical thermodynamic database for hydrated Portland cements and alkali-activated materials, Cement and Concrete Research, (2018).
[42] B. Lothenbach, L. Pelletier-Chaignat, F. Winnefeld, Stability in the system $CaO–Al_2O_3–H_2O$, Cement and Concrete Research, 42 (2012) 1621-1634.
[43] T. Mitsuda, H. Taguchi, Formation of magnesium silicate hydrate and its crystallzation to talc, Cement and Concrete Research, 7 (1977) 223-230.
[44] T. Zhang, C. Cheeseman, L. Vandeperre, Development of low pH cement systems forming magnesium silicate hydrate (MSH), Cement and Concrete Research, 41 (2011) 439-442.
[45] D.R.M. Brew, F.P. Glasser, Synthesis and characterisation of magnesium silicate hydrate gels, Cement and Concrete Research, 35 (2005) 85-98.
[46] L. Pauling, The structure of the chlorites, Proceedings of the National Academy of Sciences of the United States of America, 16 (1930) 578.
[47] S. Komarneni, C.A. Fyfe, G.J. Kennedy, H. Strobl, Characterization of Synthetic and Naturally Occurring Clays by ^{27}Al and ^{29}Si Magic‐Angle Spinning NMR Spectroscopy, Journal of the American Ceramic Society, 69 (1986).
[48] J. Sanz, J. Serratosa, Silicon-29 and aluminum-27 high-resolution MAS-NMR spectra of phyllosilicates, Journal of the American Chemical Society, 106 (1984) 4790-4793.
[49] L. Li, X. Liu, Y. Ge, R. Xu, J. Rocha, J. Klinowski, Structural studies of pillared saponite, The Journal of Physical Chemistry, 97 (1993) 10389-10393.
[50] M. Mägi, E. Lippmann, A. Samoson, G. Engelhardt, A.R. Grimmer, Solid-state high-resolution silicon-29 chemical shifts in silicates, The Journal of Physical Chemistry, 88 (1984) 1518-1522.
[51] E. Lippmaa, A. Samoson, M. Magi, High-resolution aluminum-27 NMR of aluminosilicates, Journal of the American Chemical Society, 108 (1986) 1730-1735.
[52] C. Bisio, G. Gatti, E. Boccaleri, L. Marchese, G. Superti, H. Pastore, M. Thommes, Understanding physico–chemical properties of saponite synthetic clays, Microporous and Mesoporous Materials, 107 (2008) 90-101.
[53] D. Costenaro, G. Gatti, F. Carniato, G. Paul, C. Bisio, L. Marchese, The effect of synthesis gel dilution on the physico-chemical properties of acid saponite clays, Microporous and Mesoporous Materials, 162 (2012) 159-167.
[54] T. Hibino, A. Tsunashima, Characterization of repeatedly reconstructed Mg− Al hydrotalcite-like compounds: Gradual segregation of aluminum from the structure, Chemistry of materials, 10 (1998) 4055-4061.
[55] J.W. Gruner, The crystal structures of talc and pyrophyllite, Zeitschrift für Kristallographie-Crystalline Materials, 88 (1934) 412-419.
[56] I. Dódony, M. Pósfai, P.R. Buseck, Revised structure models for antigorite: An HRTEM study, American Mineralogist, 87 (2002) 1443-1457.
[57] J. Jones, Al–O and Si–O tetrahedral distances in aluminosilicate framework structures, Acta Crystallographica Section B: Structural Crystallography and Crystal Chemistry, 24 (1968) 355-358.

[58] C.E. White, J.L. Provis, T. Proffen, D.P. Riley, J.S. van Deventer, Combining density functional theory (DFT) and pair distribution function (PDF) analysis to solve the structure of metastable materials: the case of metakaolin, Physical Chemistry Chemical Physics, 12 (2010) 3239-3245.
[59] S.J. Billinge, M. Kanatzidis, Beyond crystallography: the study of disorder, nanocrystallinity and crystallographically challenged materials with pair distribution functions, Chemical communications, (2004) 749-760.
[60] J.T. Kloprogge, Spectroscopic Methods in the Study of Kaolin Minerals and Their Modifications, Springer2019.
[61] W.A. Deer, R.A. Howie, J. Zussman, Rock-forming minerals: orthosilicates, Volume 1A, Geological Society of London, 1982.
[62] H. Saalfeld, M. Wedde, Refinement of the crystal structure of gibbsite, A1 (OH) 3, Zeitschrift für Kristallographie-Crystalline Materials, 139 (1974) 129-135.
[63] K. Gong, C.E. White, Nanoscale Chemical Degradation Mechanisms of Sulfate Attack in Alkali-activated Slag, The Journal of Physical Chemistry C, 122 (2018) 5992-6004.
[64] C. Roosz, P. Vieillard, P. Blanc, S. Gaboreau, H. Gailhanou, D. Braithwaite, V. Montouillout, R. Denoyel, P. Henocq, B. Madé, Thermodynamic properties of CSH, CASH and MSH phases: Results from direct measurements and predictive modelling, Applied Geochemistry, 92 (2018) 140-156.
[65] D.A. Palmer, P. Bénézeth, D.J. Wesolowski, Aqueous high-temperature solubility studies. I. The solubility of boehmite as functions of ionic strength (to 5 molal, NaCl), temperature (100–290 C), and pH as determined by in situ measurements, Geochimica et Cosmochimica Acta, 65 (2001) 2081-2095.
[66] J. Haas, A. Nonat, From C–S–H to C–A–S–H: Experimental study and thermodynamic modelling, Cement and Concrete Research, 68 (2015) 124-138.
[67] J.D. Miller, J. Nalaskowski, B. Abdul, H. Du, Surface characteristics of kaolinite and other selected two layer silicate minerals, The Canadian Journal of Chemical Engineering, 85 (2007) 617-624.